

Peroxymonosulfate Activated by Amorphous Particulate MnO₂ for Mineralization of Benzene Gas: Redox Reaction, Weighting Analysis, and Numerical Modelling

Haiwei Li^a, Shuncheng Lee^{a,*}, Zuwu Wang^b, Yu Huang^c, Wingkei Ho^d, Long Cui^a

^a Department of Civil and Environmental Engineering, The Hong Kong Polytechnic University, Hong Kong, China

^b Department of Environmental Engineering, Wuhan University, Wuhan 430079, China

^c Key Lab of Aerosol Chemistry&Physics, Institute of Earth Environment, Chinese Academy of Science, Xi'an 710075, China

^d Department of Science and Environmental Studies and Centre for Education in Environmental Sustainability, The Hong Kong University of Education, Hong Kong, China

* Corresponding author at: ZS943, Block Z, The Hong Kong Polytechnic University, Hung Hom, Kowloon, Hong Kong, China

E-mail address: ceslee@polyu.edu.hk

Abstract

Amorphous particulate MnO_2 (AMO) which features micro-nano hierarchical structure can be viewed as a favorable alternative to crystalline $\alpha\text{-MnO}_2$ for Peroxymonosulfate (PMS) activation. The former not only is comparatively simple to obtain but also has similar performance on powerful adsorption and catalytic capability. In this paper, the combined use of AMO and PMS oxidizing system showed the paralleled degradation efficiency of benzene gas with $50.5\pm 3.75\%$, which was just around 5 percentage points lower than that achieved in the $\alpha\text{-MnO}_2$ &PMS system. Highly stable catalytic activity of the AMO&PMS system exhibited during an ensuing cyclic experiment, averaging at 63.08% for benzene mineralization. Additionally, a novel method of weighting analysis which evaluates the synergetic effects among operating parameters on benzene removal was firstly explored in the nanosized catalyst-based activation system. Through a novel specific reaction drag model for porous media, specific drag coefficients at various testing conditions, k_2 , in terms of pressure drop across microporous AMO, were held to establish the correlations between ideal mineralization efficiencies and optimal parameter combinations. A further comparison between laboratory data and model simulations confirmed that, regardless of pH variations, the mineralization rate can be enhanced to around 67.7% at a more higher temperature (45 °C) when the consumed ratio of AMO to PMS leveled off at 0.8, during which time much lower k_2 of 0.24 Pa·min·m/mg would present.

Keywords

Amorphous particulate MnO_2 ; Peroxymonosulfate; Benzene gas; Mineralization;

Weighting analysis; Numeric model

1. Introduction

Apart from oxygen radicals (i.e., hydroxyl radicals $\bullet\text{OH}$ and superoxide radicals $\bullet\text{O}_2^-$) mostly emerged in the advanced oxidation processes (AOPs), sulfate radicals ($\text{SO}_4\bullet^-$) with a stronger redox potential of 2.5 ~ 3.1 V have been studied as another major oxide to degrade a wide range of organic compounds in wastewater purification and soil remediation, such as carbonyls, chlorophenols, and polycyclic aromatic hydrocarbons [1-5]. There are two basic persulfate anions to be activated to generate sulfate radicals, one is persulfate (PS), and the other is PMS. In liquid-phase oxidation system, some properties of persulfate that are high water solubility, chemical stability, and benign residual results make it attracted in the in-situ chemical oxidations [4, 6]. Comparatively, PMS, in the form of Oxone, outperforms more powerful oxidizing capability than persulfate and Fenton reagents due to its higher activity when transition metals as activator are presented [7-9]. Compared with UV radiation, heat, or electrostatics for the activation of PS or PMS, the transition metal ions like Ru(IV), Co(II), Zn(II), and Mn(IV) have been commonly tested as qualified catalysts for the sulfate radicals production [10-15]. Nevertheless, the high cost, toxic nature, and metal leaching or loss of Ru(IV) and Co(II) can induce severe secondary pollution and health problems, thus limiting their commercialization [7, 11]. MnO_2 , which is much abundant in nature, not only can become an efficient activator for the catalyst-mediated decomposition of PMS, but also can be used as a catalytic support to aggregate and precipitate target contaminants because of its very tiny nano-based structure [7, 8]. According to different inter-link ways of MnO_6 octahedra, MnO_2

exists several major crystallographic phases, α -, β -, γ - MnO_2 with 1D tunnels whereas λ - MnO_2 with 3D spinal structure [15-19]. Many previous studies have focused their much attention on combined use α - MnO_2 and PMS to degrade refractory organic compounds, because α - MnO_2 is characteristic of high surface area, oxygen loss, and double tunneled structure exhibits the highest activity for PMS activation [7, 8, 20, 21]. However, synthesis of nano-crystalline α - MnO_2 is followed through a time-consuming hydrothermal route, during which time crystal dimensionality, size, and structure of the final products largely depend on the complicated hydrothermal conditions, including higher temperature (190 °C), pH range, pressure, and ions concentration (i. e., NH_4^+ and SO_4^{2-}) [17]. But recently, AMO has been found to present the paralleled performance with α - MnO_2 on the refractory organic degradation, though α - MnO_2 outperforms AMO on the heterogeneous PMS activation [22]. With MnO_4^- or Mn^{2+} as the main Mn source, AMO can be directly obtained through a simple liquid-phase oxidation under the mild laboratory conditions [22-25]. Since its powerful negative charge storages and dominant heterogeneous surface process (i.e., hydrogen evolution reaction and oxygen evolution reaction) [26], AMO was extensively focused on its desirable adsorptive potential for the decomposition of aqueous compounds such as phenolic compounds, amines, heterocyclic compounds, heterocyclic N-oxides, and antibiotics. Therefore, AMO as a promising alternative for PMS activation presents not only superior catalytic activity, but also cheap, extensive pH range, and environmentally friendly.

Actually, few studies have attached their enough attention on PMS activation by

AMO and removal of gaseous contaminants by the PMS-based oxidizing system. Gaseous benzene, a typical kind of refractory volatile organic compounds (VOCs), is a major indoor air contaminant causing severe health risks for a long-term exposure ($20\text{ }\mu\text{g}/\text{m}^3$ above 14 days) and becomes a key precursor of secondary organic aerosols (SOAs) and photo-chemical smog [27]. In this study, the morphology and structure properties of AMO nanoparticles were systematically characterized and the oxidation processes of benzene by the AMO&PMS oxidizing system were firstly investigated. The obtained AMO exhibited highly efficient for strong adsorptive removal and enhanced degradation for benzene under the presence of PMS.

Additionally, although the mineralization efficiencies of benzene by the AMO&PMS system were promising, the synergetic effects among different operating parameters on the mineralization are still not completely clarified. As for the complex heterogeneous catalytic oxidation incurred among AMO particles, PMS solutions, and benzene gas, data contributing of each operating parameter (i. e., temperature, pH, or reactant concentration) in spite of subtle variations would exert remarkable influence on the oxide consumptions and decontaminating results. To further probe the feasibility of the AMO&PMS system for highly-enhanced benzene removal, weighting analysis (contributions) of parameters is a necessary method of searching the optimization solutions of the testing conditions (parameter combinations). Unlike conventional weighting methods like P-Value or Response Surface Methodology (RSM) [28, 29] which have been proven not difficult but rather tedious, a novel specific reaction drag model for weighting analysis was developed to hold specific

drag coefficient k_2 in terms of pressure drop when benzene flowed across a newly-built microporous media. In other words, the heterogeneous reactions at various testing conditions resulted in pressure variations and existed different specific drag coefficients k_2 , which can be used to reflect the significant levels of the weighting analysis to the mineralization efficiencies. A comparative investigation between laboratory measurements and Computational Fluid Dynamics (CFD) simulations of the specific drag model eventually confirmed that k_2 would become a favorable weighting factor to establish the correlations between various operating conditions and mineralization efficiencies in the AMO&PMS oxidizing system.

2. Experimental section

2.1. Chemicals

PMS ($\text{KHSO}_5 \cdot 0.5\text{KHSO}_4 \cdot 0.5\text{K}_2\text{SO}_4$, > 95% purity) was obtained from Sigma-Aldrich. Synthesis of AMO was followed a redox procedure: solutions contained colloidal MnO_2 particulate (below 2 mM) or suspended MnO_2 particulate (between 5 and 30 mM) which was subjected to be a major role in the PMS activation. The suspended MnO_2 (30 mM) was prepared by stoichiometrically mixing 300 mL of KMnO_4 (0.1 M) with 112.5 mL of $\text{Na}_2\text{S}_2\text{O}_3$ (0.1 M) and diluted to 1 L with deionized water (18 M Ω) under stirring 12 h. Before drying at 70 °C, the AMO products were not washed and centrifugation with ultrapure water until kept their supernatant clean. A nickel foam was soaked in its synthesized solutions for several seconds to collect the AMO particles. Nano-crystalline α - MnO_2 was obtained through a hydrothermal reaction route where Mn^{2+} and $\text{S}_2\text{O}_8^{2-}$ coexisted [17], described in the Supporting Text

(Text S1).

2.2. Experimental procedure

An AMO&PMS oxidizing system (Fig. 1) consists of three major sections, a mass flow controller of benzene span gas, an AMO&PMS catalytic oxidation reactor, and a real-time analytical system. For the catalytic oxidation of benzene, benzene gas from its cylinder was diluted by N₂ and its desired concentrations were metered through a mass flow controller (Brooks 5860E). The reactor is a kind of semibatch modes, where benzene gas flowed into it continuously while the AMO&PMS solutions therein were stationary. The oxidizing process was carried out in a 1 L round-bottom flask, and the solutions' temperatures were maintained by a thermostatic water bath. The initial pH of PMS solutions leveled at 5.2 before the addition of AMO and pH values were adjusted by diluted H₂SO₄ (0.1 M) and NH₃ (0.1 M). A real-time benzene gas detector (Tiger Select-0512) was used to record the outlet concentrations of benzene gas whereas a TVOC analyzer (ppbRAE 3000) for the measurement of residual gaseous organic carbon products after reaction.

The pressure data acquisition system was also displayed in the inset graph of Fig.1. An 8 mm height cylinder-shaped activated carbon (AC) layer made of activated charcoal fibers (T300-3K, Toray) was fixed in a beaker with diameter 12.4 cm instead of the flask, and was situated at 12 mm below the surface of the solutions. The newly-built AC layer set as porous media aimed to simplify the data logging of pressure drop for numerical study on the weighting analysis. Since the suspended particulate AMO characterized a very tiny nanostructure similarly to a typical

microporous material, as-synthesized AMO powders (sieved to 60 ~ 80 mesh) were simultaneously injected into the AC layer through a compressed air micro-needling manipulation. For establishing the specific reaction drag model, the layer was solely used to build up a porous media, which helped to record pressure drops across the layer at various operating conditions. Prior to measurements, the blank values of pressure drop for calibration in the AC layer were monitored under pure N₂ atmosphere and were subtracted from pressure data of each testing condition. Through a conical diffuser, benzene gas can completely flow across the layer. In order to enhance the solubility of benzene gas into the reaction solutions, it was processed to keep the vacuum degree of 0.08 MPa in the mass flow controller. Two probes (PT2330-M20, ISO) fixed separately at above and below the AC layer were used to detect the current signals in terms of pressure drop, ΔP . ADAM-4018 module (trade name of Advantech, USA) then transported the current signals to ADAM-4520 isolated RS-232 to RS-485 converter module, which automatically converted the current signals to digital signals. The digital signals were finally outputted by the specific C/C++ analysis software written in a data analyzer. Thus, the values of ΔP generated from the ensuing redox reactions were achieved by a real-time analog-to-digital conversion and were used to calculate the reaction drags.

2.3. Analysis

As seen in Text S2, the crystalline phases and morphology of as-synthesized MnO₂ catalysts were characterized by X-ray diffraction (XRD, a Philips X'pert PRO SUPER diffractometer using Cu K α (λ = 0.15406 nm) radiation at 40 kV and 40 mA

with a scanning rate of 0.04°/s in the 2θ range of $10^\circ \sim 80^\circ$) and scanning electron microscopy (SEM, JEOL JSM-6490), respectively. The Brunauer-Emmett-Teller (BET) surface area of as-prepared samples was obtained from N_2 adsorption/desorption isotherms at 77 K by using a Gemini VII 2390 automatic analyzer (Text S3). Electron spin-resonance spectroscopy (ESR, ER200-SRC, Bruker, Germany) was also used for the determination of the production and intensity of free radicals. X-ray photoemission spectroscopy (XPS) was recorded on a Thermo ESCALAB 250 system which all the binding energies were calibrated to the C 1s peak at 284.8 eV of the surface adventitious carbon.

Reaction solutions were sampled at predetermined time intervals and excessive $HONH_3Cl$ was then injected into samples to quench the reaction. The residual concentrations of AMO and PMS were determined by UV-vis spectrophotometry (Text S4, a Varian Cary 100 Scan UV-Visible system equipped with a labsphere diffuse reflectance accessory) and iodometric titration, respectively [30]. The degradation rate of benzene was noted as $1-(C_t/C_0)$, where C_t is the benzene concentration of the outlet at any given time, and C_0 is the initial concentration; while the mineralization rate was calculated by $1-\{[TVOC]_t/[TVOC]_0\}$, the $[TVOC]_0$ and $[TVOC]_t$ in the formula are the concentration of organic carbon compounds at an initial and any given time, respectively.

Highly precise measurements (repeatability) of the inlet concentration of benzene gas enable initial transitional boundary conditions [31] (low-Reynolds fluids, shown in Table 1) to keep as low deviations as possible in CFD stimulations. The replicate

predetermined measurements (Text S5) were achieved by a gas chromatography with flame ionization detector (GC-FID, Agilent HP6890A). Therefore, the inlet concentration was set at 200 ppm.

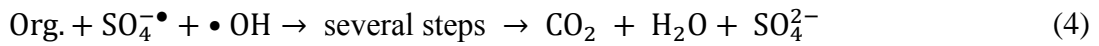
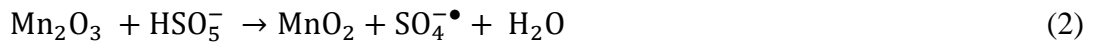
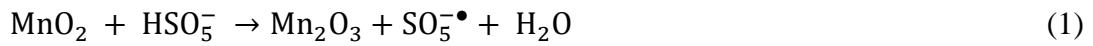
3. Results and discussion

3.1. Catalytic oxidation of benzene

Previous study reported that the electrocatalytic activities of manganese oxides followed in a descending order: α -MnO₂, AMO, β -MnO₂, γ -MnO₂ [26]. But in the comparative tests for various MnO₂ materials as shown in the inset graph of Fig. 2, AMO had the strongest capability for benzene adsorption largely due to its unique sea urchin nanostructure. Detailed information on the adsorption experiments can be found in Text S6. Besides, the benzene degradation of 4.8 mM AMO in the presence of 9.6 mM PMS achieved a second highest rate of $50.5 \pm 3.75\%$ but slightly lower than $55.3 \pm 4.14\%$ of nano-crystalline α -MnO₂, followed by only $12.7 \pm 3.52\%$ micron-sized commercial MnO₂. Many investigators [8, 16, 26] ascribed the highest PMS activation of α -MnO₂ to its double-tunneled structure and high specific capacitance ($240 \text{ F} \cdot \text{g}^{-1}$), supplying enough negative charges for the generation cycles of sulfate radicals; while the higher porosity ($0.19 \text{ cm}^3/\text{g}$) and greater surface area ($157.71 \text{ m}^2/\text{g}$) of AMO also strengthen the charge mobility.

Fig. 2 also displays that, with combined use of AMO and PMS, benzene degradation was much higher, ranging from 60.0% to 66.5%, than their individual use as pH of the reaction solutions increased from 2.5 to 9. This observation means that the combined oxidizing system for benzene degradation was not restricted by different

pH levels, but also was far beyond the degradation rate from the sum of their individual use. Eqs. (1) ~ (4) [22, 32] account for the extensive pH range of the AMO&PMS system. The formation of sulfate radicals $\text{SO}_4^{\cdot-}$ and hydroxyl radicals $\cdot\text{OH}$ is enhanced under alkaline conditions in the PMS system. $\cdot\text{OH}$ would offset the depletion of $\text{SO}_4^{\cdot-}$. But $\text{SO}_4^{\cdot-}$ recover in the transition cycles of Mn ions at neutral or weak pH [1]; while the production of hydroxyl radicals largely relies on the first order kinetics as a function of temperature with a lower activation energy [7, 8]. ESR spectra and radical scavenge experiments (Text S7) reveal that benzene was predominantly and durably oxidized with $\text{SO}_4^{\cdot-}$, because a gradual depletion of $\cdot\text{OH}$ did not significantly induce a decrease in degradation efficiency.



The transitional reactions of manganese oxides were further investigated by the XPS spectra (Text S8) of Mn 2p_{3/2} of AMO catalysts. The chemical states of Mn oxides mainly exhibited Mn³⁺ and Mn⁴⁺; while no Mn²⁺ species appeared because the absence of a satellite peak at +5 eV from the Mn 2p_{3/2} peak [33, 34]. High relative ratios of Mn⁴⁺/Mn³⁺ implies the manganese oxides can sustain Mn content at higher oxidation states in the transitional reactions. Mn oxides at both Mn³⁺ and Mn⁴⁺ can activate PMS to produce sulfate radicals ($\text{SO}_4^{\cdot-}$ and $\text{SO}_5^{\cdot-}$). However, due to the higher activity than $\text{SO}_5^{\cdot-}$, $\text{SO}_4^{\cdot-}$ play the major reactive species for the contaminant

decomposition [26].

Fig. 3 shows the effect of AMO and PMS dose in the combined oxidizing system on the mineralization of benzene. In general, as temperature of the reaction solutions and consumed oxidants rising, the activation of PMS and the mineralization of benzene increased gradually, indicating the combined system for benzene degradation was a typical endothermal procedure but excessive high temperature could counteract the mineralization results unless the oxides are largely overdosed [35]. Increasing AMO concentrations not only improved the mineralization rate of benzene, but also contributed to the activation of PMS (Fig. 3a). Although the consumed ratio of AMO to PMS (consumed AMO/PMS) leveled off at around 0.8 after 2.9 mM AMO dose, the temperature from 35 to 45 °C helped the mineralization rate from 61.1% to the highest 67.7%. In the reaction solutions meanwhile, the radical-radical termination reactions of $\text{SO}_5^{\cdot-}$ enhanced the PMS consumption in the presence of AMO and continued to generate the strong oxidizing capability $\text{SO}_4^{\cdot-}$ in the transition cycles between Mn(III) and Mn(IV). By contrast, as PMS dose went to a higher level, the mineralization rates considerably increased because sufficient PMS was activated by AMO (Fig. 3b). When PMS dose increased beyond 4.4 mM, just 2.9 mM AMO addition experienced a rapid consumption for PMS activation. The consumed AMO/PMS appeared a similar downward trend until to stand stably at around 0.8, implying that the activation equilibrium between AMO and PMS was already achieved. Under the circumstances, higher temperature at 45 °C enabled the mineralization efficiency to reach as high as 65.7%. Therefore, once the consumed

AMO/PMS was close to 0.8 at 45 °C, the highest mineralization rate can be obtained. Noticeably, the mineralization efficiencies of benzene by the AMO&PMS oxidizing system were comparatively higher than its benzene degradation (Fig. 2), indicating that most of the mineralization contributions resulted from the conversion of intermediate products of benzene [8, 25, 36]. In order to probe the stability of activity in the AMO&PMS system for benzene mineralization, a cyclic experiment was carried out during 5 ensuing 36-min reaction periods and the period interval was set to 10 min until the flowmeter of benzene restarted. As shown in Fig. 4, the mineralization efficiencies averaged at 63.08% in the 3 h recycling reaction without an obvious decline in activity.

3.2. Optimization of AMO&PMS process

3.2.1. Weighting analysis by a novel numeric model

Since the suspended particulate AMO features a very tiny nanostructure as well as a catalytic support, the bi-component system can be viewed as a kind of typical microporous materials. A novel weighting analysis for the benzene mineralization was established by a specific drag model for porous media. During the benzene decontamination, different testing conditions resulted in different specific drag coefficients k_2 , in terms of pressure drop across the media. The coefficients were determined by the drag model and reflected the weighting impacts of parameters on the mineralization efficiencies.

As for investigations of pressure drop across a porous component, the Darcy equation extrapolates the momentum coefficients (i. e., inertial resistance factor C_2

and viscous inertial resistance factor $\frac{1}{\alpha}$). Rather than to consider distinctive topographies and inventory durations inside porous media, it approximately simulates pressure variations by a filtered fluid in the x, y, z directions (3-D) at a fixed surface velocity via Eqs. (5) and (6) [37, 38]. But if across the nanostructure AMO particles in the AC layer which were involved in a cycle of valence-electron transition and also a porous capture in the benzene mineralization, the pressure variations between the heterogeneous fluids (i. e., AMO&PMS solutions and benzene gas) would result from mass adsorption and flow retention, in addition to the decomposition and penetration of reactant molecules when the catalytic oxidations start. These factors influence pressure drop but the complicated pressure variations are not completely clarified by just pressure drop.

$$\Delta P = -\left(\sum_{j=1}^3 D_{ij} \mu v_j + \sum_{j=1}^3 C_{2ij} \frac{1}{2} \rho_f |v| v_j\right) \text{ (Pa)} \quad (5)$$

$$\Delta P = -\left(\frac{\mu}{\alpha} v_i + C_2 \frac{1}{2} \rho |v| v_j\right) \text{ (Pa)} \quad (6)$$

Using the Kozeny-Carman equation [39, 40], the most well-known permeability-porosity relation for porous media, a drag model can be described by the following equations:

$$S = k_2 W + S_E \text{ [Pa/(m/min)]} \quad (7)$$

$$S = \frac{\Delta P}{v} \text{ [Pa/(m/min)]} \quad (8)$$

where S is the total reaction drag (quotient of ΔP and v), S_E is the effective residual drag, W is the mass density of benzene gas across the AC layer, and k_2 is the specific drag coefficient [41, 42]. In our findings, S_E is the sum of three terms: the drag due to heterogeneous reactions, the drag due to disordered dispersion when reactants are

adsorbed onto the surface of the catalytic support, and the drag due to residual retention caused by insufficient reactions or unbalanced adsorption. S_E is the y-incept of the linear regression of the drag equations and simplify the description of the complex fluid dynamics in porous media. Nevertheless, S_E is rarely determined from laboratory measurements [42]. The slope k_2 , which demonstrates the reaction drags in terms of pressure drop when such operating parameters as airflow rate, mass loading, properties of reactants, etc. are involved.

The Eq. (7) is further facilitated by if concentration of benzene gas, c , is constant, so that ck_2 becomes the slope of the equation when drag is plotted versus the cumulative volume $\int \frac{Q}{A} dt$. W is then changed to the Eq. (9), where c is given in milligram per cubic meter, Q the gas volumetric flow rate in cubic meter per minute, and A the surface area of the porous zone in square meter, where the layer is assumed to be fully filled with AMO&PMS solutions:

$$W = \int c \frac{Q}{A} dt = c \int \frac{Q}{A} dt \quad (\text{mg/m}^2) \quad (9)$$

The reaction drag model can also be rewritten as,

$$S = S_E + ck_2 \int \frac{Q}{A} dt \quad [\text{Pa}/(\text{m}/\text{min})] \quad (10)$$

The nanostructure AMO catalyst has been deposited and supposed to provide a sufficient catalytic support for PMS in the AC layer. The pressure variations generated in the AC layer are displayed along 3-D distribution. For the differential analyses on the surface porous zone with uneven topography, if there are assumed N different infinitesimal areas, the Eq. (9) is further developed to the following relation:

$$W_\gamma = c \frac{\sum_{\eta=1}^3 v_\eta A_\eta}{\sum_{\gamma=1}^3 A_\eta} = c \frac{\sum_{\eta=1}^3 v_\eta}{N} = c \sum V \quad (\text{mg/m}^2) \quad (11)$$

The cumulative volume $\sum V$ describes the unstable flow velocity instead of surface velocity across porous media in an ensuing process of data logging. The final format of the model is finalized as:

$$S = ck_2 \sum V + S_E \text{ [Pa/(m/min)]} \quad (12)$$

Fig. 5 shows the approach used to determine the value of k_2 at a selected testing condition. The one-minute intervals data were recorded for a total of 90 min with inlet Q at 0.1 L/min. A linear equation of the drag model that can hold k_2 was derived. The portion of the plot of drag S versus $\sum V$ was not linear from experimental data shown by black circles, were excluded from the regression analysis primarily due to the unstable fluid dynamics towards different directions; whereas the data judged to be linear, in which S was plotted versus $\sum V$, were included in the regression analysis, shown by red circles. By the linear regression, the values of k_2 and S_E can be calculated, assumed PMS and benzene to sufficiently fill and react with nanostructure AMO catalyst inside the AC layer after $\sum V$ at $0.15 \text{ m}^3/\text{m}^2$.

The major challenge of using Darcy momentum relations [43, 44] is that the resistance factors are determined by empirical data because the pressure variations towards different directions in a porous zone are tough to express by laboratory measurements. Compared to resistance coefficients (i. e., C_2 and $\frac{1}{\alpha}$) of the Darcy equation (shown in Table 1 and Fig. 6) in different combinations of testing parameters, benzene gas across the AC layer can be seen as an approximate viscous-fluid flow. The deviations between k_2 values and absolute sums of C_2 and $\frac{1}{\alpha}$ were significant and k_2 can more precisely reflect the pressure variations when the testing conditions varied:

around 1:2 additions of AMO to PMS led to the highest efficiencies of benzene mineralization meanwhile 0.24 Pa/(m/min) of k_2 presented at a comparatively low level, instead of the reaction drags increased by the insufficient or overdose additions. The morphology and internal structure of the internal AC layer also displayed distinctive at different k_2 and supported the above observations (Text S9): the more sufficient reactions between AMO&PMS solutions and benzene gas, the less internal mass resistance.

Table 1. Comparisons of specific drag coefficient k_2 and momentum coefficients (pH = 3.6, T = 45 °C)

No.	AMO (mM)	PMS (mM)	Solutions ρ_s (g/m ³)	ϕ	μ_m	C_2	$1/\alpha$	k_2
1	2.9	1.45	473	0.097	0.0665	0.0423	176	7.46
2	1.2	2.4	469	0.081	0.0655	0.0426	178	5.59
3	0.9	5.8	960	0.150	0.0697	0.0208	168	2.25
4	1.9	5.8	1047	0.172	0.0711	0.0191	164	1.49
5	2.9	5.8	1134	0.195	0.0724	0.0176	161	0.24
6	3.9	5.8	1221	0.217	0.0738	0.0164	158	0.21
7	5.8	5.8	1308	0.240	0.0751	0.0153	155	2.07

3.2.2. CFD modelling results

The contour of the porous zone was displayed by the longitudinal section of the AC layer. A preliminary model programing of target dynamic functions for the specific reaction drag (final format, Eq. (12)) was needed in the algorithms module.

Regardless of inertial mass loss of benzene airflow, the brief context of the programing followed as: begin with inlet velocity of benzene airflow as an initial boundary condition for microporous media, propose convergence simulations of the reaction drag ascribed by both the suspended particulate AMO adsorption and dispersion and the heterogeneous reactions, then assume unstable airflow velocity would yield cumulative flow during the retention periods of the reactions.

Simulations of the specific reaction drag at various testing conditions were shown in Fig.7. Once the combination of oxide concentrations (2.9 mM AMO and 5.8 mM PMS) was provided under pH = 3.6 and T = 35 °C, the contour region of reaction drag magnitude at $1.2 \sim 1.5 \times 10^3$ Pa/(m/min) rapidly narrowed to the center of the porous zone; while the boundary of the drag magnitude transformed smooth and extended along spreading angle of the airflow. When comparing the drag magnitude in the thermal tests, the simulation result at 35 °C under fixed oxide concentrations and pH (2.9 mM AMO, 5.8 mM PMS, and pH = 3.6) presented a good repeatability. A rise of reaction temperature to 45 °C made the drag region greatly squeezed by lower-magnitude isobaric region and the highest-magnitude drag contour (red area) was also significantly decreased. Nevertheless, few variations of drag magnitude were attributed to the pH extensive range, even though $\text{SO}_4^{\bullet-}$ could be easily generated at an acid condition [7, 20].

Through comparisons between laboratory tests and model simulations, values of k_2 under various operating conditions were determined by the drag model and decreased considerably with the a gradual rise in dose of either AMO or PMS (Fig. 8).

But when ensuring the consumed AMO/PMS at around 0.8 after their adding ratio at between 1:2 and 2:3, the values of k_2 would keep a comparatively lower level of 0.21 ~ 0.24 Pa·min·m/mg and an ideal mineralization rate 66.7% of benzene was achieved. In a case where extra AMO to PMS dose can dramatically recover k_2 once the highest efficiency was already able to reach, probably due to an agglomeration of micron homogeneous particles into larger ones which were impossible to thoroughly react yet in the AC layer. Therefore, higher mineralization efficiencies correlated with lower k_2 . The reaction processes of the combined oxidizing system for benzene mineralization can be described by the reaction drag model and k_2 indicates in turn how to enhance the efficiencies through the optimization of a combination of the operating parameters. Overall, the model accomplished a precise weighting analysis of various testing conditions on the mineralization efficiencies of benzene gas in the AMO&PMS oxidizing system which used to be determined from a large amount of laboratory measurements through trial and error.

4. Conclusion

A novel bi-component oxidizing system consisting of AMO and PMS achieves a competing performance, instead of extensively studied crystalline α -MnO₂, on the mineralization of benzene gas. Since its sea urchin nanostructure with many flakes radiating from center, AMO with high BET surface areas provides a sufficient adsorptive and reactive opportunity for PMS activation. The AMO&PMS system enhances the sulfate radical-involved oxidation of benzene and intermediates degradation, approximate 67.7% mineralization efficiency and much lower reaction

drags generated as a result. This paper also provides a specific reaction drag model for optimizing the catalytic process and predicting the mineralization efficiencies of benzene gas over the AMO&PMS oxidizing system. The developed k_2 value has accomplished a precise weighting analysis of various testing conditions on the benzene removal and accounted for the synergetic effects among operating parameters on the mineralization efficiencies in terms of k_2 . The simulation results reconciled to the laboratory measurements. Comparing to other parameters like oxide concentrations and pH, an increase of temperature would realize a more thorough redox reaction of AMO&PMS with benzene gas. Consequently, a highly precise and easily handling weighting analysis, in terms of the specific reaction drag model, can establish and evaluate the optimal combinations of the operating parameters, only to make the combined oxidizing system ultimate usefulness in the pilot-scale test and industrial application.

Appendix A. Supporting text

Supporting text associated with this article can be found in this section.

Appendix B. Nomenclature

A	area of the porous zone (m^2)
C_{2ij}	inertial resistance factor
c	inlet concentration of target contaminant (mg/Nm^3)
D_{ij}	viscous resistance factor
k_2	specific drag coefficient ($\text{Pa}\cdot\text{min}\cdot\text{m}/\text{g}$)
N	different unit areas of uneven topography in porous media
Q	volumetric flow rate (m^3/h)

S	specific reaction drag [Pa/(m/min)]
S_E	effective residual drag [Pa/(m/min)]
$v_{i,j}$	velocity across porous media toward i,j directions (m/s)
W	areal density of porous media (g/m ²)
ΔP	pressure drop (Pa)
ΣV	cumulative flow (m ³ /m ²)

Greek symbols

$\frac{1}{\alpha}$	viscous inertial resistance factor
μ	dynamic viscosity (Pa·s)
μ_m	viscosity of suspended/colloidal-phase fluid (mm ² /s)
ρ_f	density of fluid (g/m ³)
ρ_s	density of AMO&PMS solutions (g/m ³)
φ	volume fraction of disperse phase

Acknowledgements

This study was supported by The National Key Research and Development Program of China (2016YFA0203000), The National Science Foundation of China (41573138), Research Grants Council of Hong Kong Government (PolyU152083/14E and PolyU152090/15E), Hong Kong RGC Collaborative Research Fund (C5022-14G), and the Ministry of Science and Technology (2013FY112700). We also thank senior architect Mr. Tianyi Dong (Shenyang Tianhua Architecture Design Institute, China) for supporting in model simulations of the reaction drags.

References

- [1] Y.H. Guan, J. Ma, X.C. Li, J.Y. Fang, L.W. Chen, Influence of pH on the formation of sulfate and hydroxyl radicals in the UV/peroxymonosulfate system,

Environ. Sci. Technol., 45 (2011) 9308-9314.

- [2] G. Fang, J. Gao, D.D. Dionysiou, C. Liu, D. Zhou, Activation of persulfate by quinones: free radical reactions and implication for the degradation of PCBs, Environ. Sci. Technol., 47 (2013) 4605-4611.
- [3] Y. Yang, J. Jiang, X. Lu, J. Ma, Y. Liu, Production of sulfate radical and hydroxyl radical by reaction of ozone with peroxymonosulfate: a novel advanced oxidation process, Environ. Sci. Technol., 49 (2015) 7330-7339.
- [4] Y. Gao, Z. Zhang, S. Li, J. Liu, L. Yao, Y. Li, H. Zhang, Insights into the mechanism of heterogeneous activation of persulfate with a clay/iron-based catalyst under visible LED light irradiation, Appl. Catal. B: Environ., 185 (2016) 22-30.
- [5] Y. Ren, L. Lin, J. Ma, J. Yang, J. Feng, Z. Fan, Sulfate radicals induced from peroxymonosulfate by magnetic ferrosphenel MFe_2O_4 ($M = Co, Cu, Mn, \text{ and } Zn$) as heterogeneous catalysts in the water, Appl. Catal. B: Environ., 165 (2015) 572-578.
- [6] P. Avetta, A. Pensato, M. Minella, M. Malandrino, V. Maurino, C. Minero, K. Hanna, D. Vione, Activation of persulfate by irradiated magnetite: implications for the degradation of phenol under heterogeneous photo-Fenton-like conditions, Environ. Sci. Technol., 49 (2015) 1043-1050.
- [7] Y. Wang, S. Indrawirawan, X. Duan, H. Sun, H.M. Ang, M.O. Tadé, S. Wang, New insights into heterogeneous generation and evolution processes of sulfate radicals for phenol degradation over one-dimensional $\alpha\text{-MnO}_2$ nanostructures, Chem. Eng.

J. , 266 (2015) 12-20.

- [8] E. Saputra, S. Muhammad, H. Sun, H.M. Ang, M.O. Tade, S. Wang, Different crystallographic one-dimensional MnO_2 nanomaterials and their superior performance in catalytic phenol degradation, *Environ. Sci. Technol.*, 47 (2013) 5882-5887.
- [9] G. Ragukumar, P. Andal, M. Murugavelu, C. Lavanya, M.S. Ramachandran, Effect of metal ions on acetone dicarboxylic acid catalyzed peroxomonosulphate reactions, *J. Mol. Catal. A: Chem.*, 390 (2014) 22-28.
- [10] P.A. George, D.D. Dionysios, Radical generation by the interaction of transition metals with common oxidants, *Environ. Sci. Technol.*, 38 (2004) 3705-3712.
- [11] S. Muhammad, P.R. Shukla, M.O. Tade, S. Wang, Heterogeneous activation of peroxymonosulphate by supported ruthenium catalysts for phenol degradation in water, *J. Hazard. Mater.*, 215-216 (2012) 183-190.
- [12] Q. Yang, H. Choi, Y. Chen, D.D. Dionysiou, Heterogeneous activation of peroxymonosulfate by supported cobalt catalysts for the degradation of 2,4-dichlorophenol in water: the effect of support, cobalt precursor, and UV radiation, *Appl. Catal. B: Environ.*, 77 (2008) 300-307.
- [13] X. Duan, K. O'Donnell, H. Sun, Y. Wang, S. Wang, Sulfur and nitrogen Co-doped graphene for metal-free catalytic oxidation reactions, *Small*, 11(2015), 3036-3044.
- [14] S. Liu, W. Peng, H. Sun, S. Wang, Physical and chemical activation of reduced graphene oxide for enhanced adsorption and catalytic oxidation, *Nanoscale*, 6

(2014) 766-771.

- [15] Y. Wang, H. Sun, H.M. Ang, M.O. Tadé, S. Wang, 3D-hierarchically structured MnO_2 for catalytic oxidation of phenol solutions by activation of peroxymonosulfate: structure dependence and mechanism, *Appl. Catal. B: Environ.*, 164 (2015) 159-167.
- [16] S. Devaraj, N. Munichandraiah, Effect of crystallographic structure of MnO_2 on its electrochemical capacitance properties, *J. Phys. Chem. C*, 112 (2008) 4406-4417.
- [17] X. Wang, Y.D. Li, Synthesis and formation mechanism of manganese dioxide nanowires/nanorods, *Chem. Eur. J.*, 9 (2003) 300-306.
- [18] I. Zaharieva, M.M. Najafpour, M. Wiechen, M. Haumann, P. Kurz, H. Dau, Synthetic manganese–calcium oxides mimic the water-oxidizing complex of photosynthesis functionally and structurally, *Energ. Environ. Sci.*, 4 (2011) 2400.
- [19] A. Iyer, H. Galindo, S. Sithambaram, C. King'onde, C.H. Chen, S.L. Suib, Nanoscale manganese oxide octahedral molecular sieves (OMS-2) as efficient photocatalysts in 2-propanol oxidation, *Appl. Catal. A: Gen.*, 375 (2010) 295-302.
- [20] E. Saputra, S. Muhammad, H. Sun, A. Patel, P. Shukla, Z.H. Zhu, S. Wang, $\alpha\text{-MnO}_2$ activation of peroxymonosulfate for catalytic phenol degradation in aqueous solutions, *Catal. Commun.*, 26 (2012) 144-148.
- [21] L. Duan, B. Sun, M. Wei, S. Luo, F. Pan, A. Xu, X. Li, Catalytic degradation of Acid Orange 7 by manganese oxide octahedral molecular sieves with peroxymonosulfate under visible light irradiation, *J. Hazard. Mater.*, 285 (2015)

356-365.

- [22] S. Gao, J. Cui, Y. Xiong, W. Xiao, D. Wang, A.N. Alshawabkeh, X. Mao, Synergetic effect of the mineralization of organic contaminants by a combined use of permanganate and peroxymonosulfate, *Sep. Purif. Technol.*, 144 (2015) 248-255.
- [23] F. Joaquin, Perez-Benito, A. Conchita, A. Elisenda, A kinetic study of the reduction of colloidal manganese dioxide by oxalic acid, *J. Colloid Interface Sci.*, 177 (1996) 288-297.
- [24] Y. Yang, E. Liu, L. Li, Z. Huang, H. Shen, X. Xiang, Nanostructured amorphous MnO_2 prepared by reaction of KMnO_4 with triethanolamine, *J. Alloy. Compd.*, 505 (2010) 555-559.
- [25] D. Li, G. Shen, W. Tang, H. Liu, Y. Chen, Large-scale synthesis of hierarchical MnO_2 for benzene catalytic oxidation, *Particuology*, 14 (2014) 71-75.
- [26] Y. Meng, W. Song, H. Huang, Z. Ren, S.Y. Chen, S.L. Suib, Structure-property relationship of bifunctional MnO_2 nanostructures: highly efficient, ultra-stable electrochemical water oxidation and oxygen reduction reaction catalysts identified in alkaline media, *J. Am. Chem. Soc.*, 136 (2014) 11452-11464.
- [27] A. Luengas, A. Barona, C. Hort, G. Gallastegui, V. Platel, A. Elias, A review of indoor air treatment technologies, *Rev. Environ. Sci. Bio.*, 14 (2015) 499-522.
- [28] J. Zhou, X. Yu, C. Ding, Z. Wang, Q. Zhou, H. Pao, W. Cai, Optimization of phenol degradation by *Candida tropicalis* Z-04 using Plackett-Burman design and response surface methodology, *J. Environ. Sci.-China*, 23 (2011) 22-30.

- [29] L. Mohajeri, H.A. Aziz, M.H. Isa, M.A. Zahed, A statistical experiment design approach for optimizing biodegradation of weathered crude oil in coastal sediments, *Bioresour. Technol.*, 101 (2010) 893-900.
- [30] S. Dubey, S. Hemkar, C. Khandelwal, P. Sharma, Kinetics and mechanism of oxidation of hypophosphorous acid by peroxomonosulphate in acid aqueous medium, *Inorg. Chem. Commun.*, 5 (2002) 903-908.
- [31] A. Sohankar, C. Norberg, L. Davidson, Simulation of three-dimensional flow around a square cylinder at moderate Reynolds numbers, *Phys. Fluids*, 11 (1999) 288.
- [32] E. Saputra, S. Muhammad, H. Sun, H.M. Ang, M.O. Tadé, S. Wang, Manganese oxides at different oxidation states for heterogeneous activation of peroxymonosulfate for phenol degradation in aqueous solutions, *Appl. Catal. B: Environ.*, 142-143 (2013) 729-735.
- [33] S. Mo, S. Li, J. Li, S. Peng, J. Chen, Y. Chen, Promotional effects of Ce on the activity of Mn-Al oxide catalysts derived from hydrotalcites for low temperature benzene oxidation, *Catal. Commun.*, 87 (2016) 102-105.
- [34] X. Li, Z. Ao, J. Liu, H. Sun, R.I. Alexandre, J. Wang, Topotactic transformation of metal-organic frameworks to graphene-encapsulated transition-metal nitrides as efficient fenton-like catalysts, *ACS nano*, (2016), online accepted.
- [35] F. Wang, H. Dai, J. Deng, G. Bai, K. Ji, Y. Liu, Manganese oxides with rod-, wire-, tube-, and flower-like morphologies highly effective catalysts for the removal of Toluene, *Environ. Sci. Technol.*, 46 (2012) 4034-4041.

- [36] S. Mo, S. Li, W. Li, J. Li, J. Chen, Y. Chen, Excellent low temperature performance for total benzene oxidation over mesoporous CoMnAl composited oxides from hydrotalcites, *J. Mater. Chem. A*, 4 (2016) 8113-8122.
- [37] O. Krehel, A. Muntean, P. Knabner, Multiscale modeling of colloidal dynamics in porous media including aggregation and deposition, *Adv. Water Resour.*, 86 (2015) 209-216.
- [38] Y. Wang, M. Brannock, S. Cox, G. Leslie, CFD simulations of membrane filtration zone in a submerged hollow fibre membrane bioreactor using a porous media approach, *J. Membrane Sci.*, 363 (2010) 57-66.
- [39] C.P. Carman, *Flow of gases through porous media*, Butterworths Scientific Publications, London, 1956.
- [40] C.P. Carman, Book reviews: flow of gases through porous media, *Sci.*, 124 (1956) 1254-1255.
- [41] R.F. Heaphy, K.M. Cushing, W.A. Harrison, Improved control of primary fine particulate emissions with electrostatically augmented fabric filtration, *ICESP IX*, 2003.
- [42] H. Li, Z. Wang, Y. Ye, Z. Wang, A model analysis on the pulse-jet cleaning performance of electrostatically stimulated fabric filtration, *Powder Technol.*, 291 (2016) 499-505.
- [43] S. Whitaker, Flow in porous media I: a theoretical derivation of Darcy's law, *Transport Porous Med.*, 1 (1986) 3-25.
- [44] D. Tiab, E.C. Donaldson, *Theory and practice of measuring reservoir rock and*

fluid transport properties: chapter 3 porosity and permeability, Petrophysics
(Forth-Edition), Gulf professional publishing, 2015, pp. 67-186.

Captions to illustrations

Fig. 1. The AMO&PMS oxidizing system with a flask and the pressure data acquisition system with a beaker (inset graph).

Fig. 2. Comparisons of PMS activated by different forms of manganese dioxide (inset graph) and benzene degradation of various oxidants by individual AMO, PMS, and combined use of them ($C_{\text{AMO}} = 2.9 \text{ mM}$, $C_{\text{PMS}} = 5.8 \text{ mM}$, $T = 45 \text{ }^{\circ}\text{C}$).

Fig. 3. Mineralization of benzene, consumed AMO and PMS as a function of AMO dose (a) and mineralization of benzene, consumed AMO and PMS as a function of PMS dose (b) under different temperatures of the reaction solutions.

Fig.4. Stability of activity in the AMO&PMS oxidizing system for benzene mineralization ($\text{pH} = 3.6$, $T = 45 \text{ }^{\circ}\text{C}$, $C_{\text{AMO}} = 2.9 \text{ mM}$, $C_{\text{PMS}} = 5.8 \text{ mM}$).

Fig. 5. Reaction drag model used to determine specific drag coefficient k_2 ($\text{pH} = 3.6$, $T = 45 \text{ }^{\circ}\text{C}$, $C_{\text{AMO}} = 2.9 \text{ mM}$, $C_{\text{PMS}} = 5.8 \text{ mM}$).

Fig. 6. Significant deviations between k_2 and momentum coefficients.

Fig.7. Comparisons of specific reaction drag at various operating conditions: blank test of the AC layer in pure N_2 atmosphere (a); $C_{\text{AMO}} = 1.9 \text{ mM}$ (b); $C_{\text{AMO}} = 2.9 \text{ mM}$ (c); $C_{\text{AMO}} = 3.9 \text{ mM}$ (d); $T = 25 \text{ }^{\circ}\text{C}$ (e); $T = 35 \text{ }^{\circ}\text{C}$ (f); $T = 45 \text{ }^{\circ}\text{C}$ (g); $\text{pH} = 2.5$ (h); $\text{pH} = 3.6$ (i); $\text{pH} = 7$ (j).

Fig. 8. Effects of model results k_2 at various consumed ratios of AMO to PMS on benzene mineralization (in an ensuing 90 min data logging, $\text{pH} = 3.6$, $T = 45 \text{ }^{\circ}\text{C}$).

Fig. 1

[Click here to download high resolution image](#)

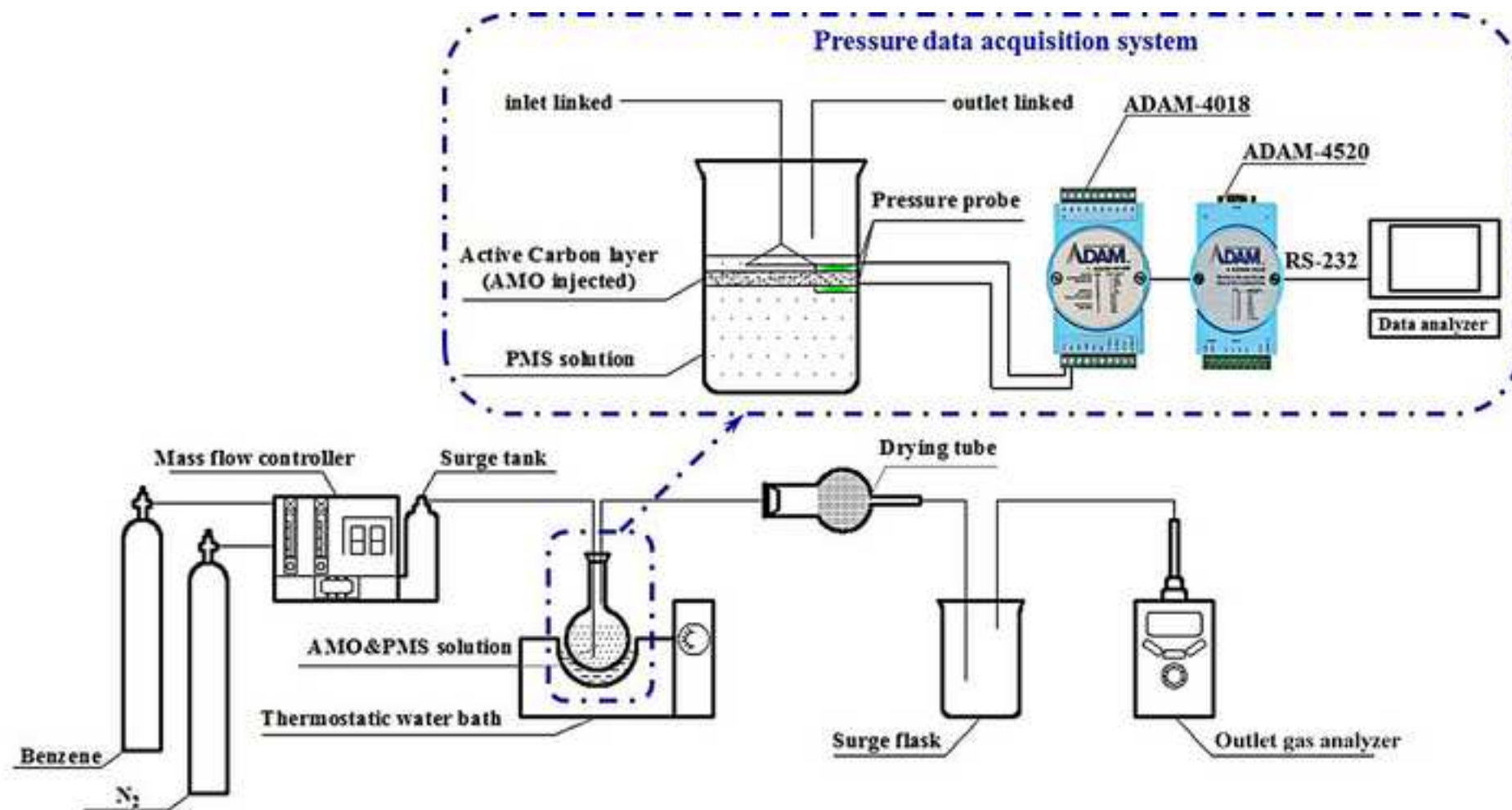


Fig. 2
[Click here to download high resolution image](#)

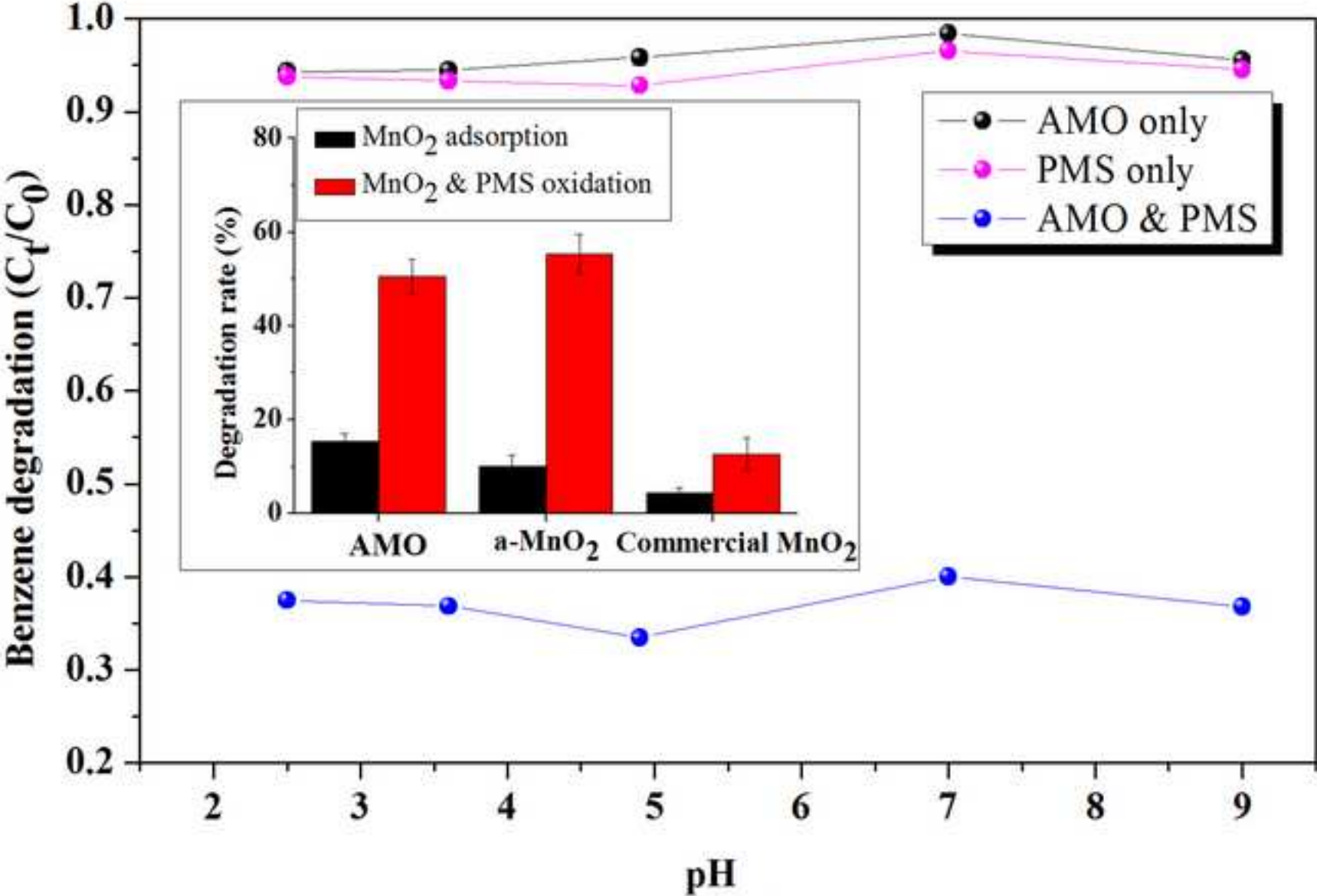


Fig. 3.a

[Click here to download high resolution image](#)

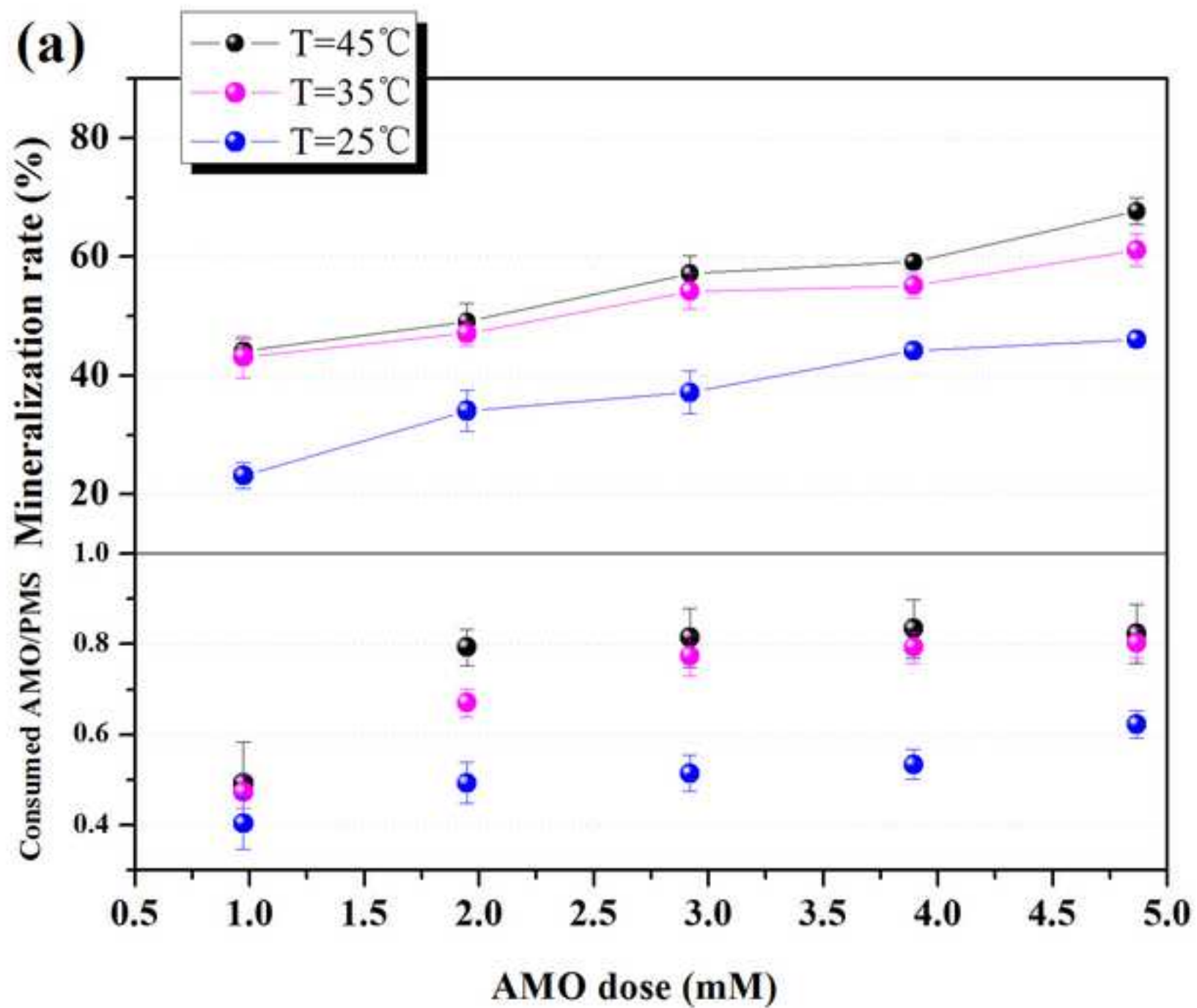


Fig. 3.b

[Click here to download high resolution image](#)

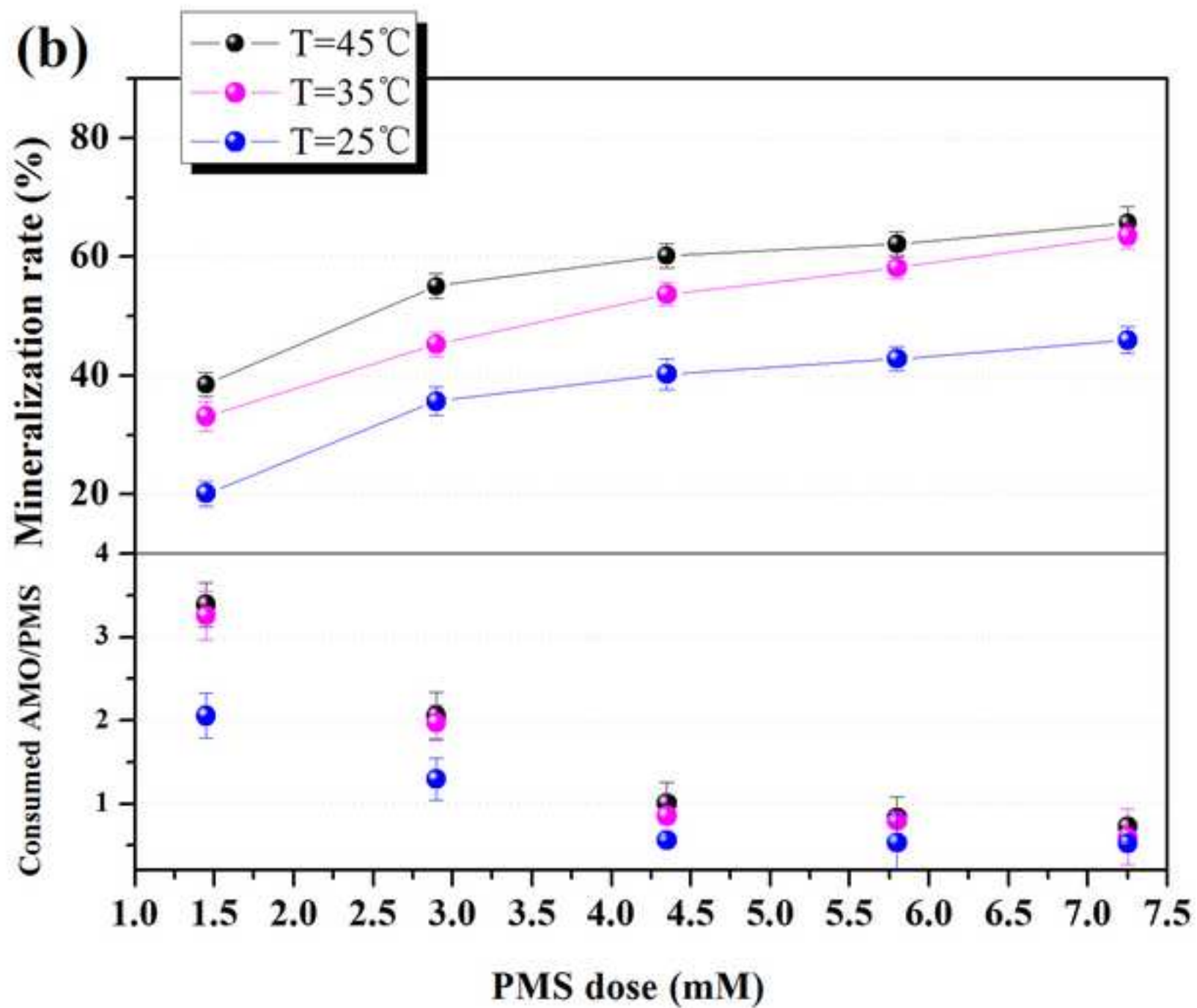


Fig. 4

[Click here to download high resolution image](#)

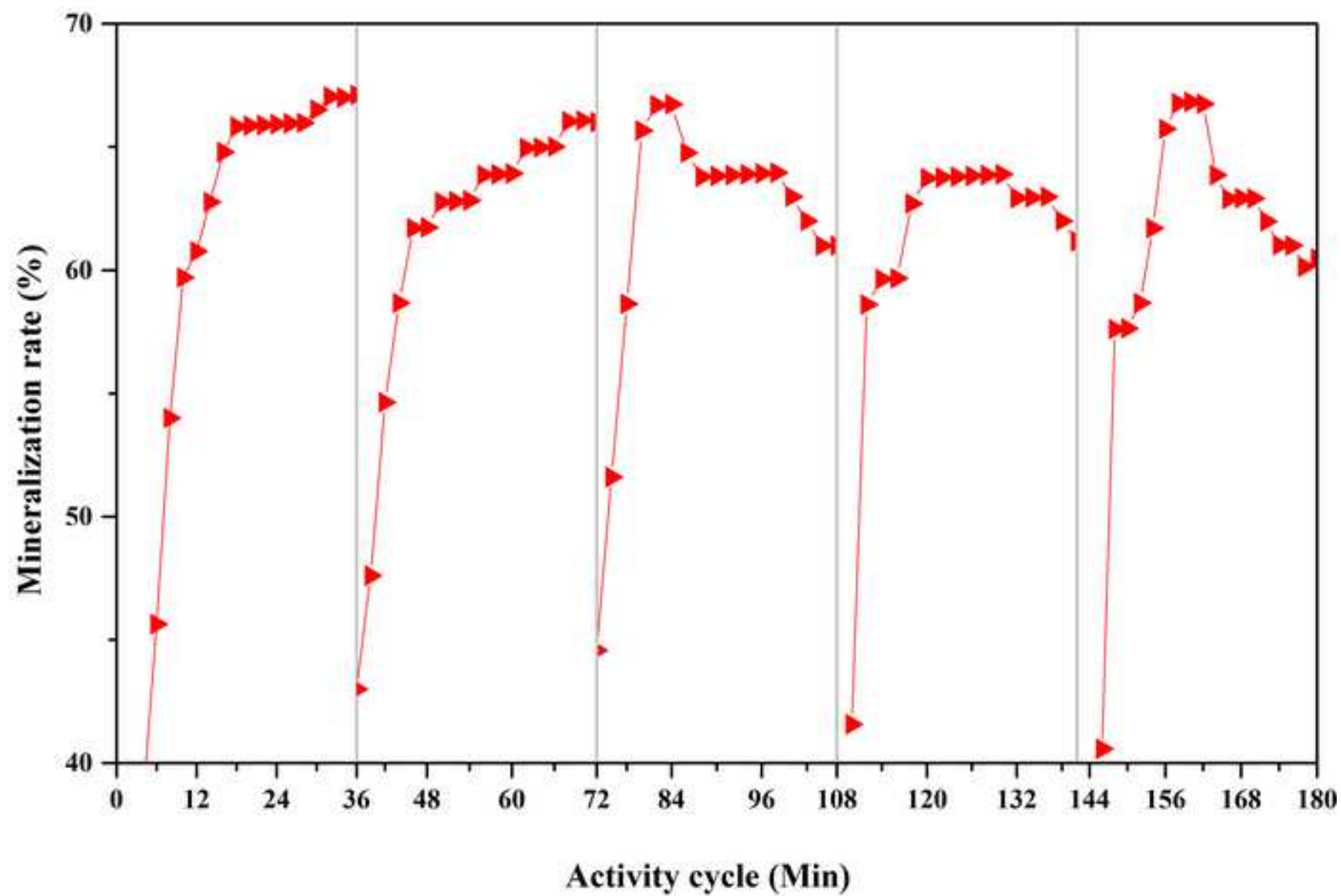


Fig. 5

[Click here to download high resolution image](#)

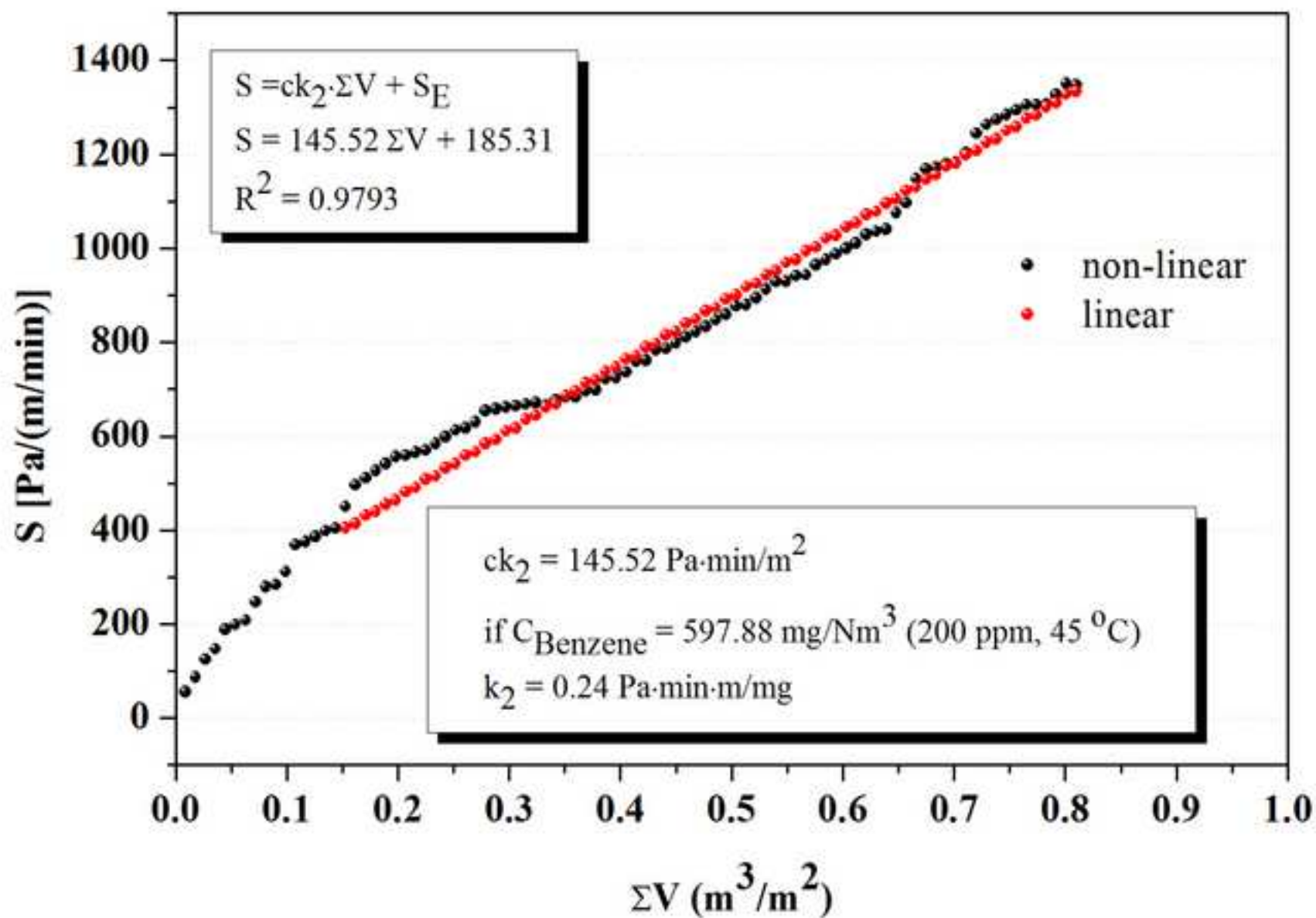


Fig. 6

[Click here to download high resolution image](#)

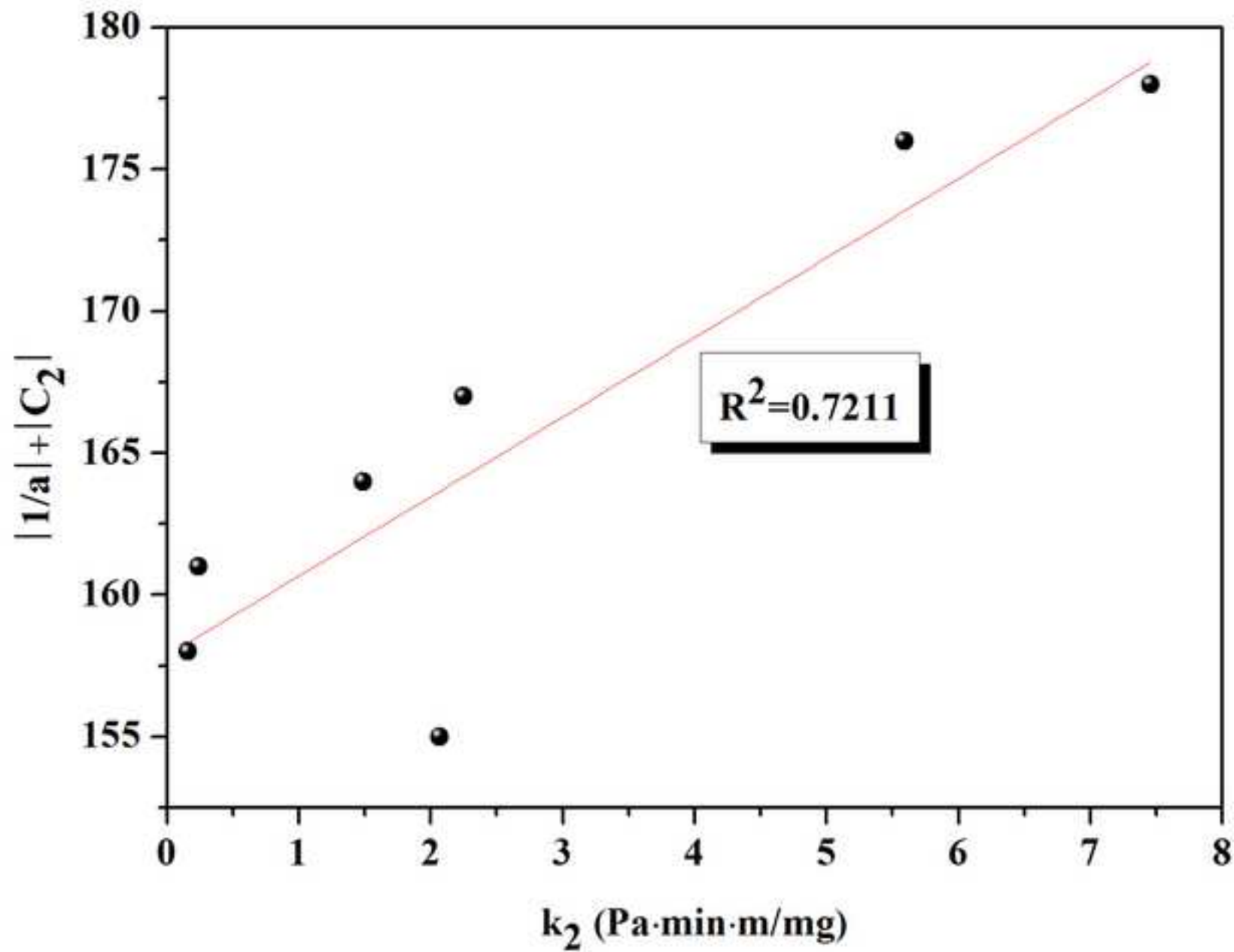


Fig. 7
[Click here to download high resolution image](#)

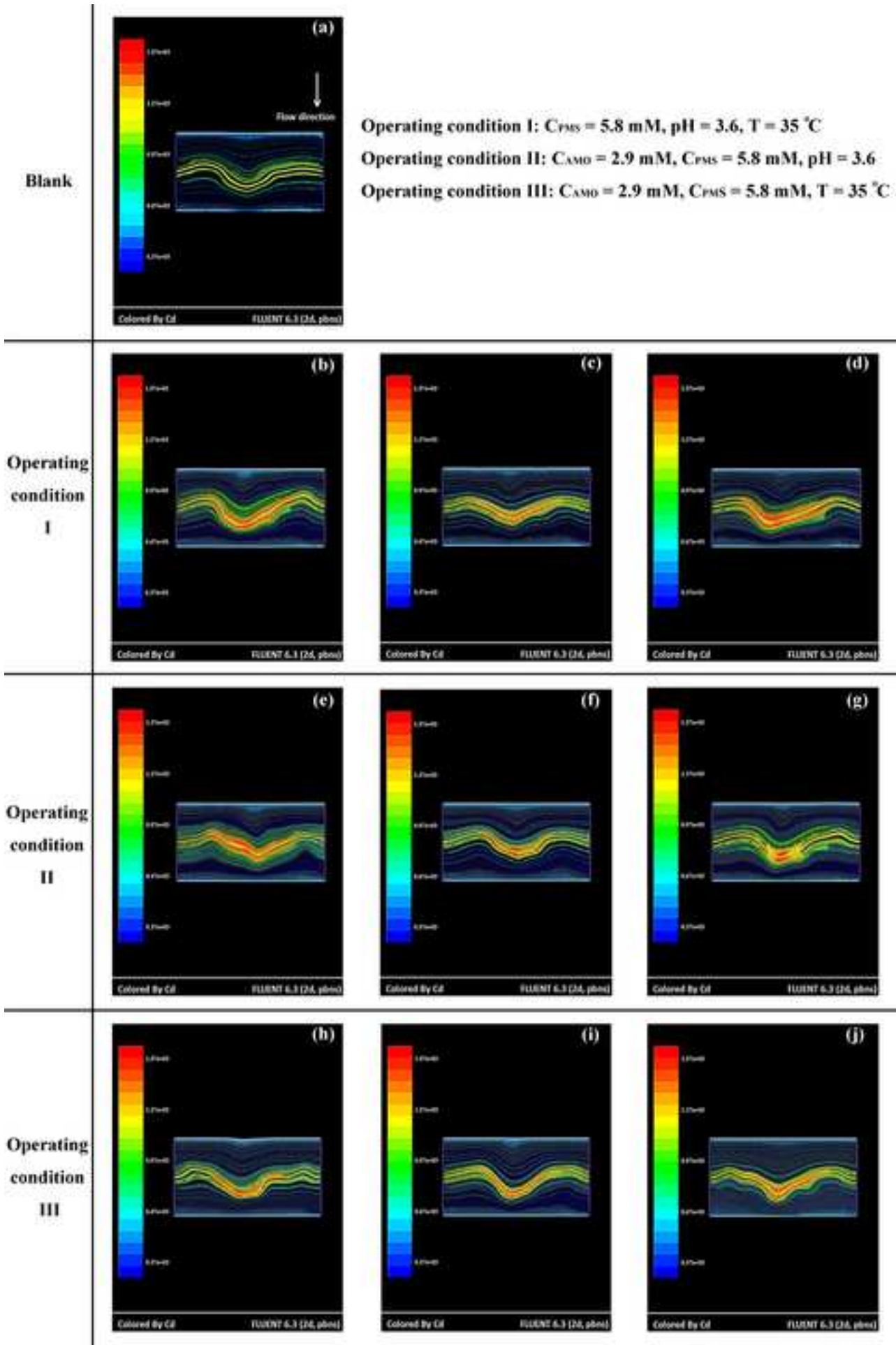


Fig. 8

[Click here to download high resolution image](#)

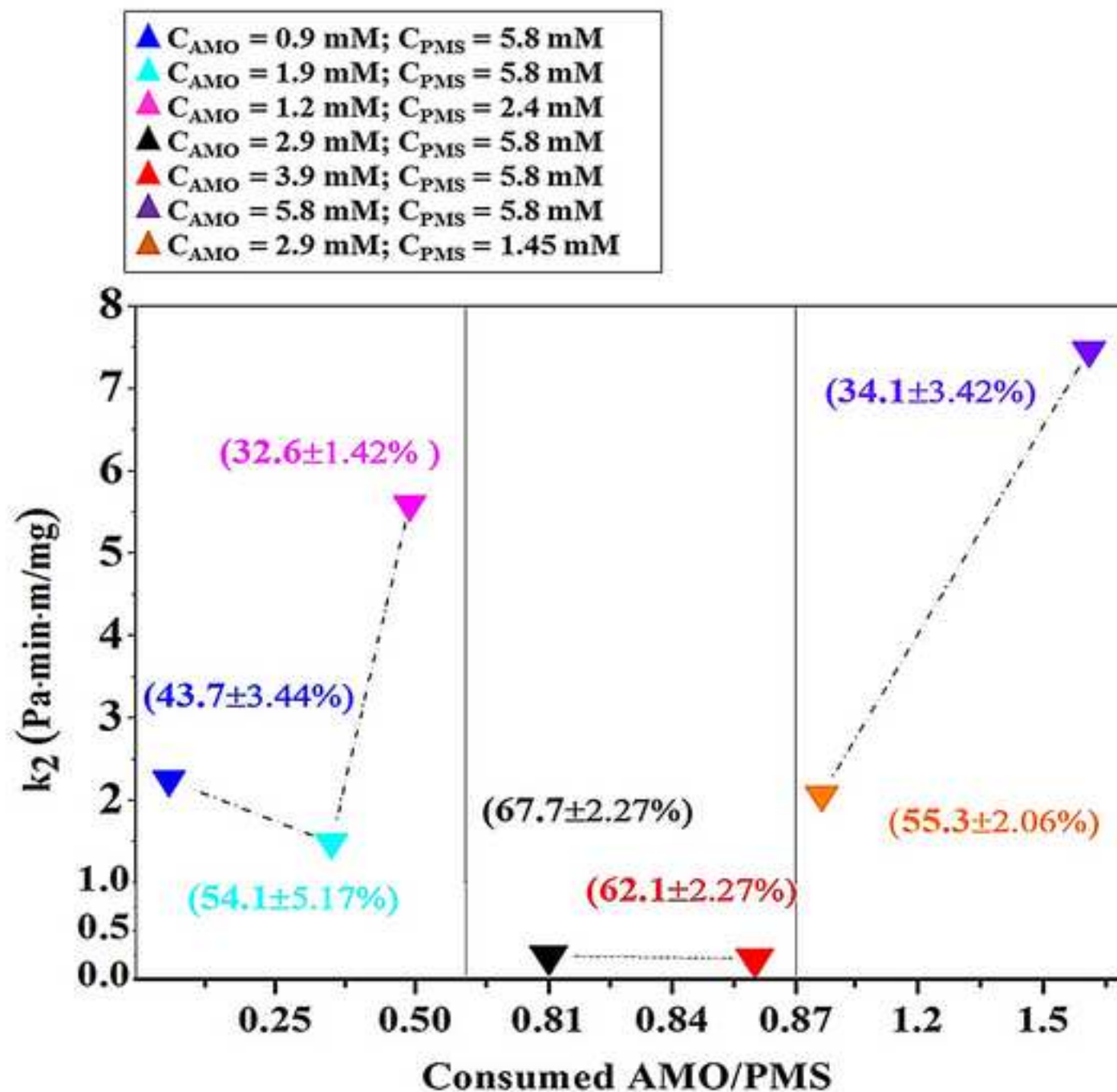


Fig. S1

[Click here to download high resolution image](#)

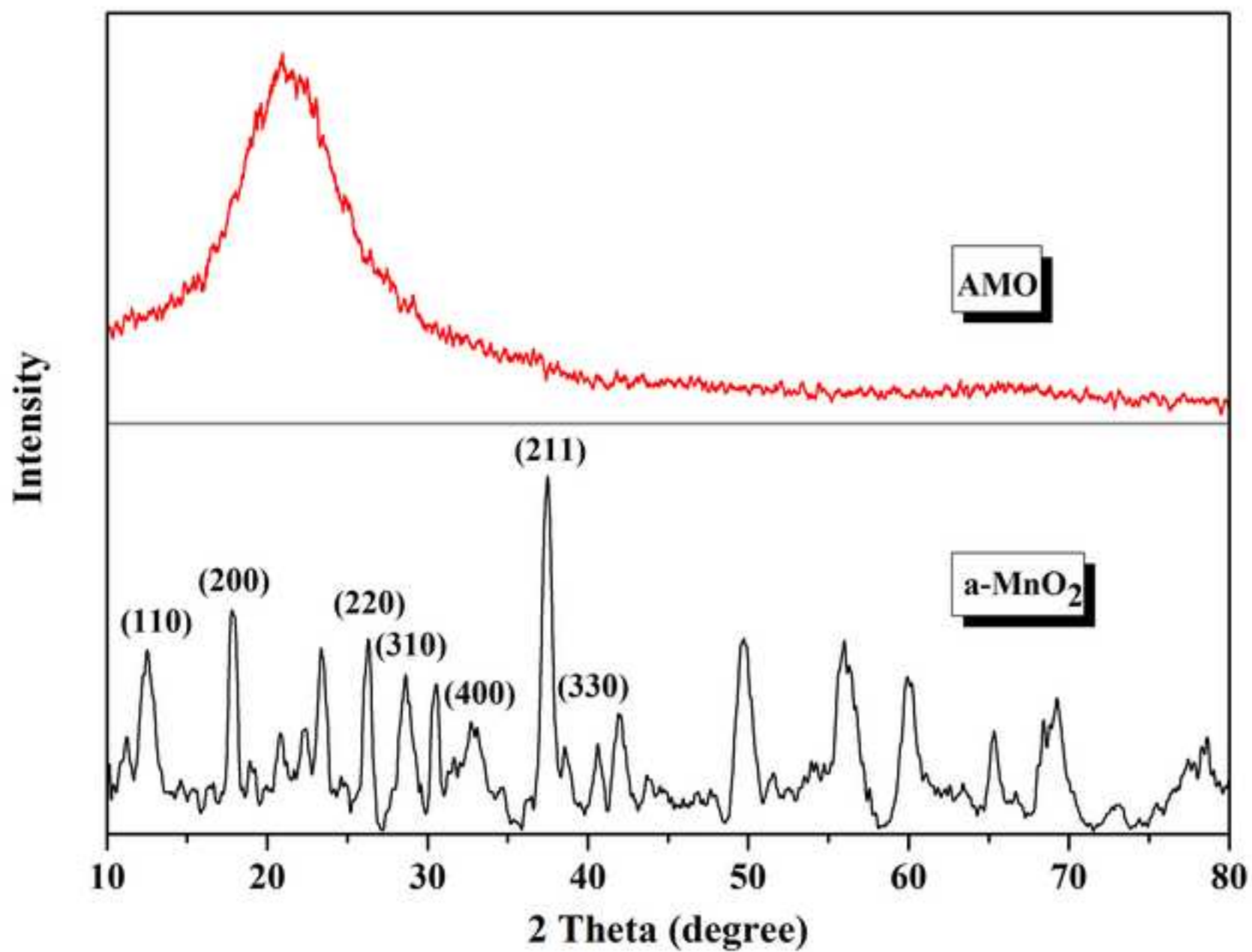


Fig. S2.a
[Click here to download high resolution image](#)

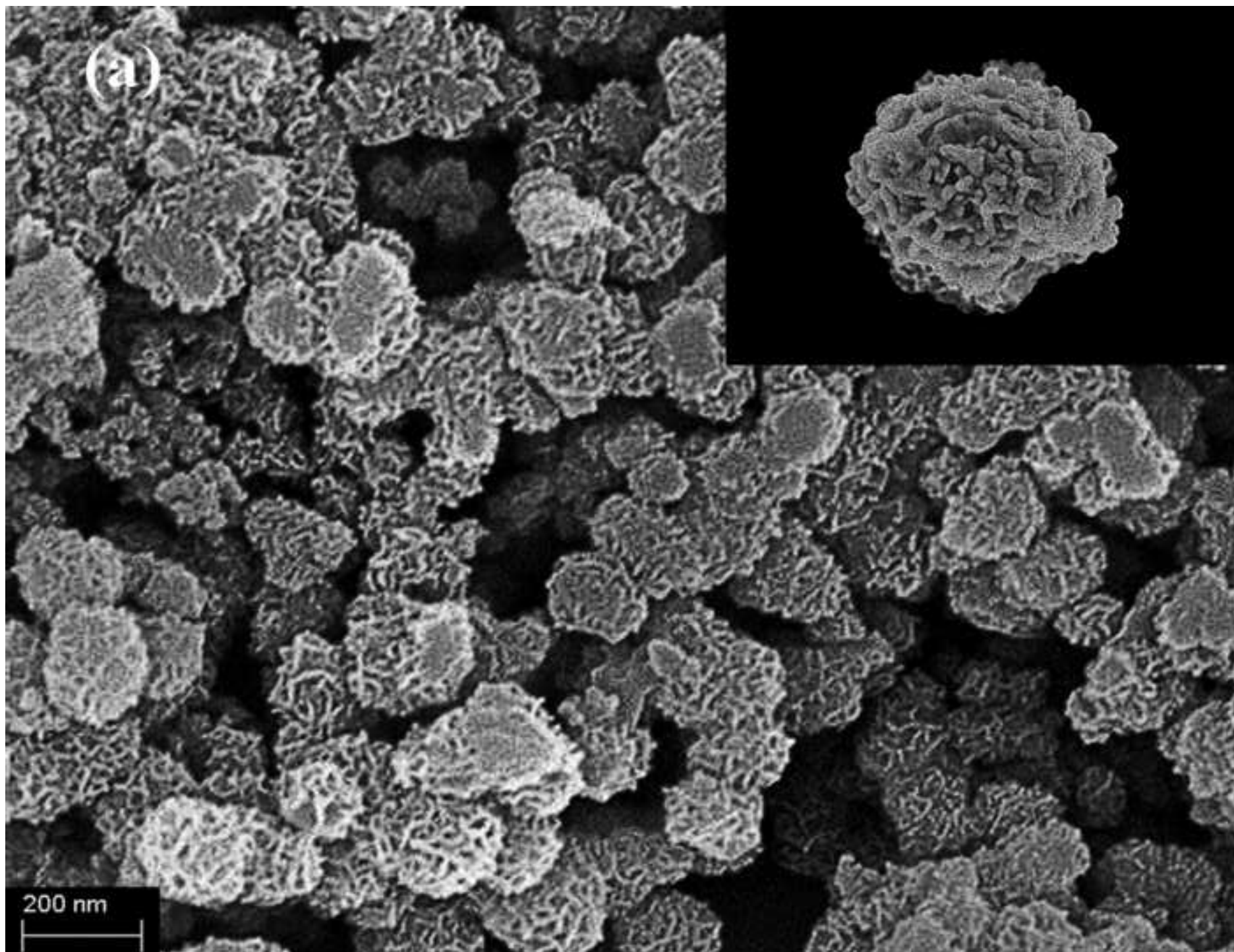


Fig. S2.b
[Click here to download high resolution image](#)

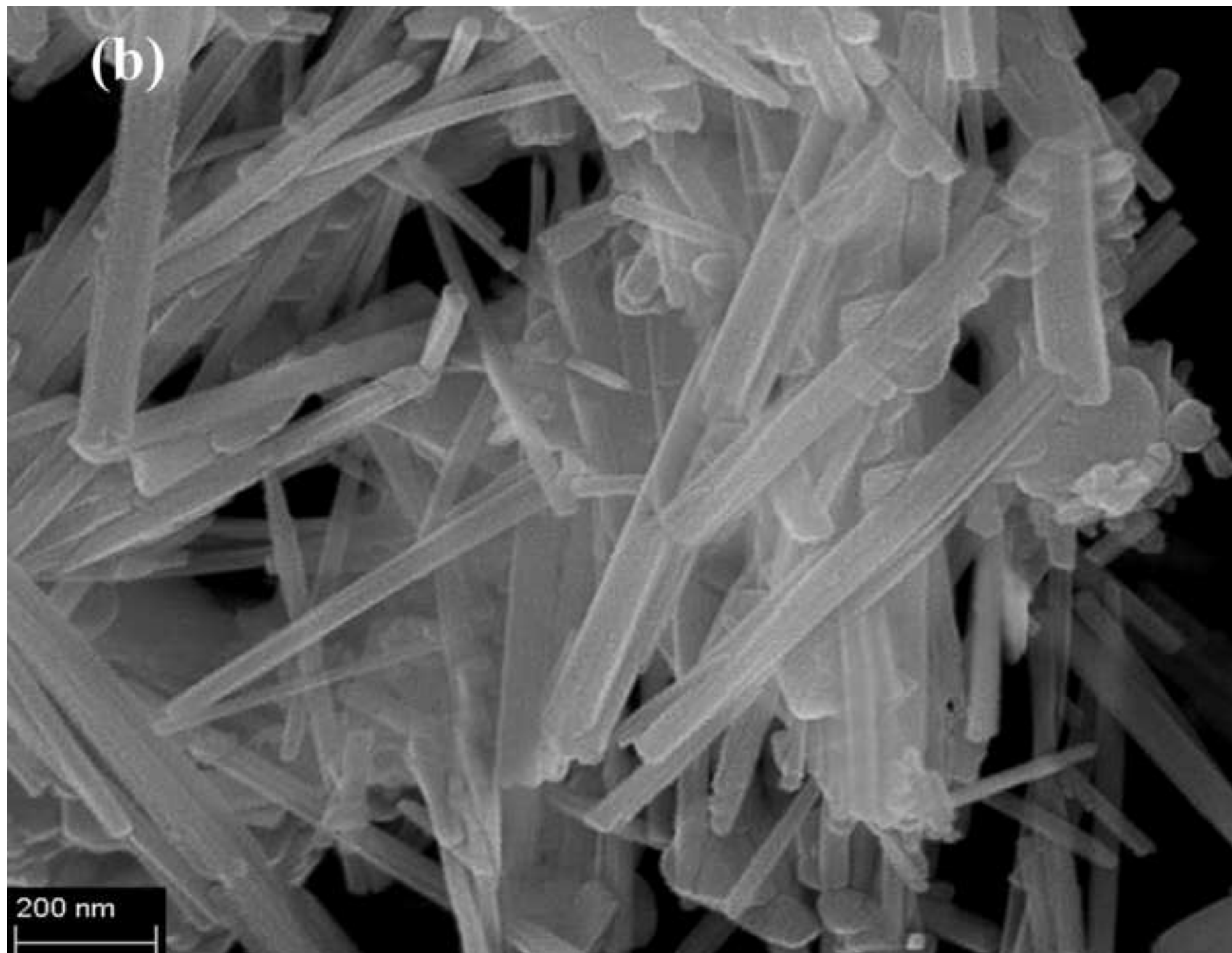


Fig. S3.a

[Click here to download high resolution image](#)

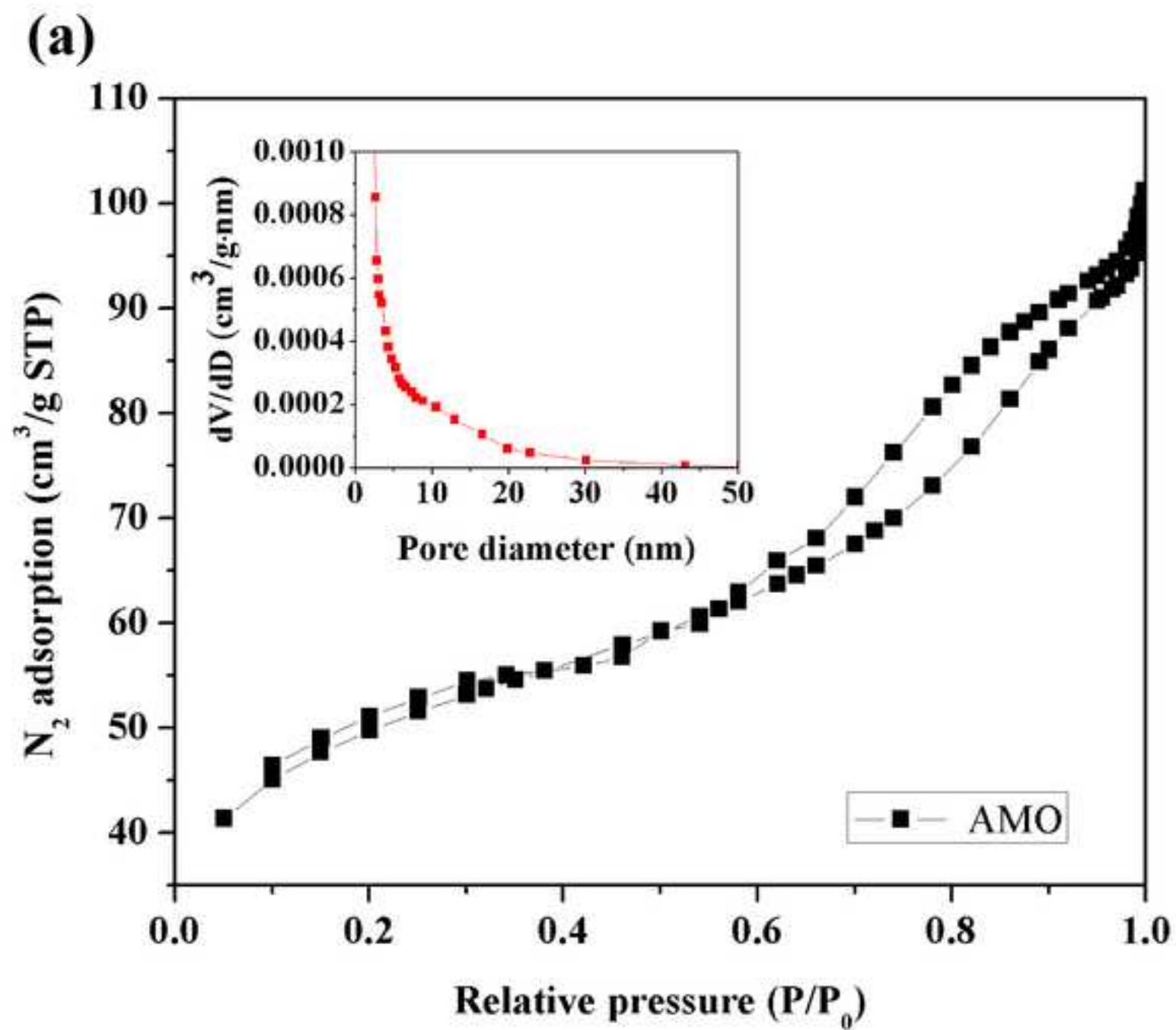


Fig. S3.b

[Click here to download high resolution image](#)

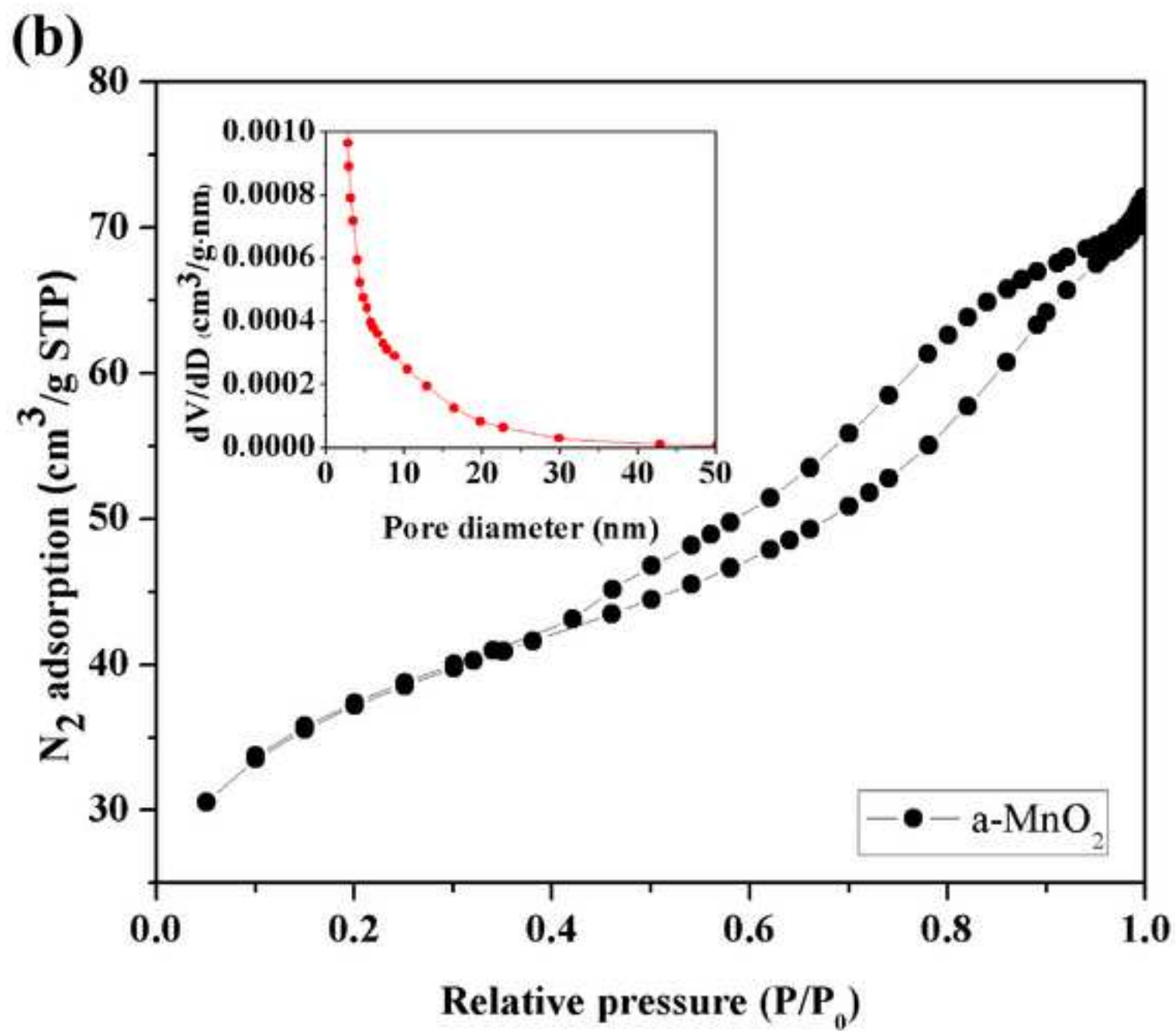


Fig. S4

[Click here to download high resolution image](#)

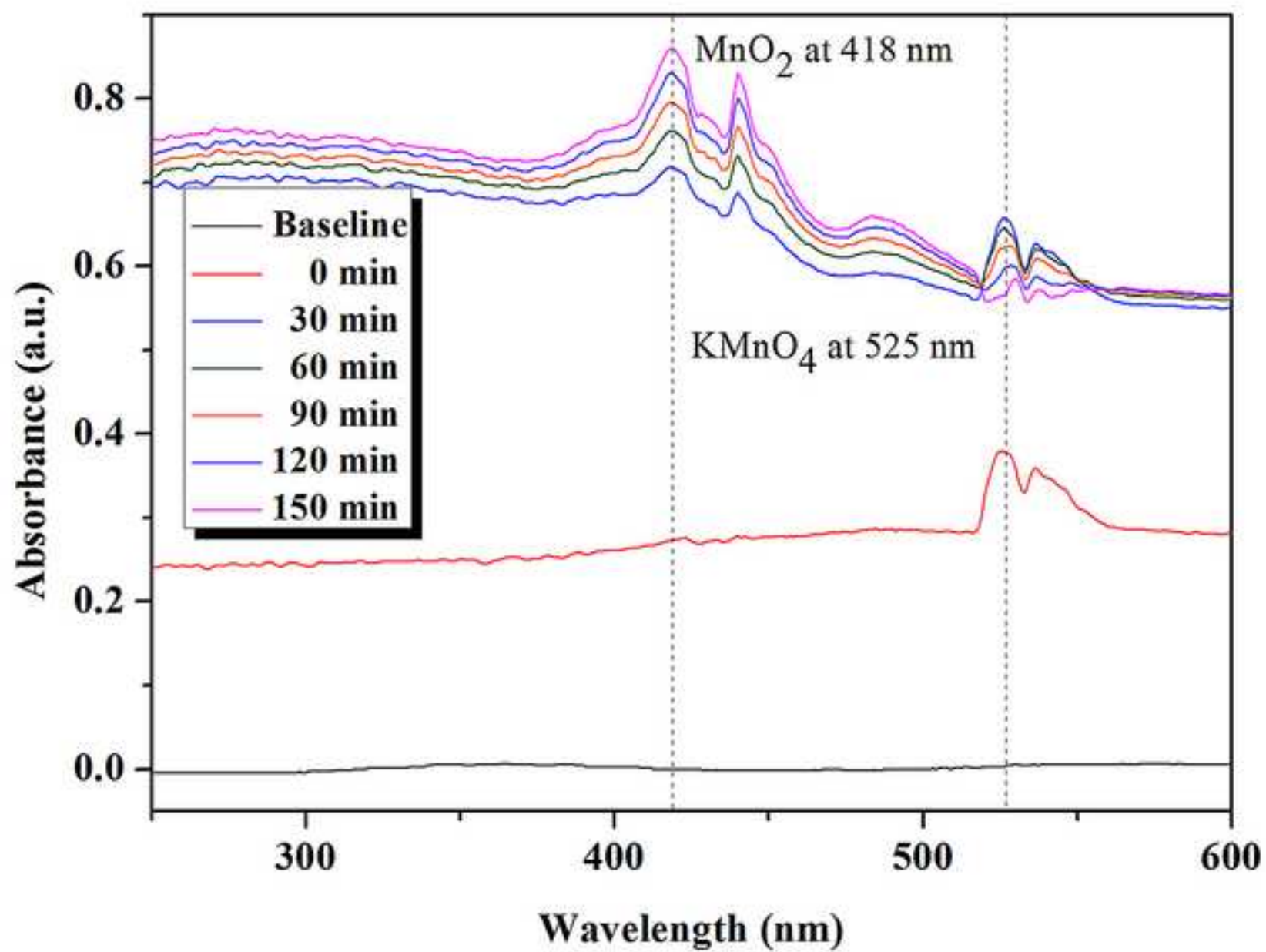


Fig. S5.a

[Click here to download high resolution image](#)

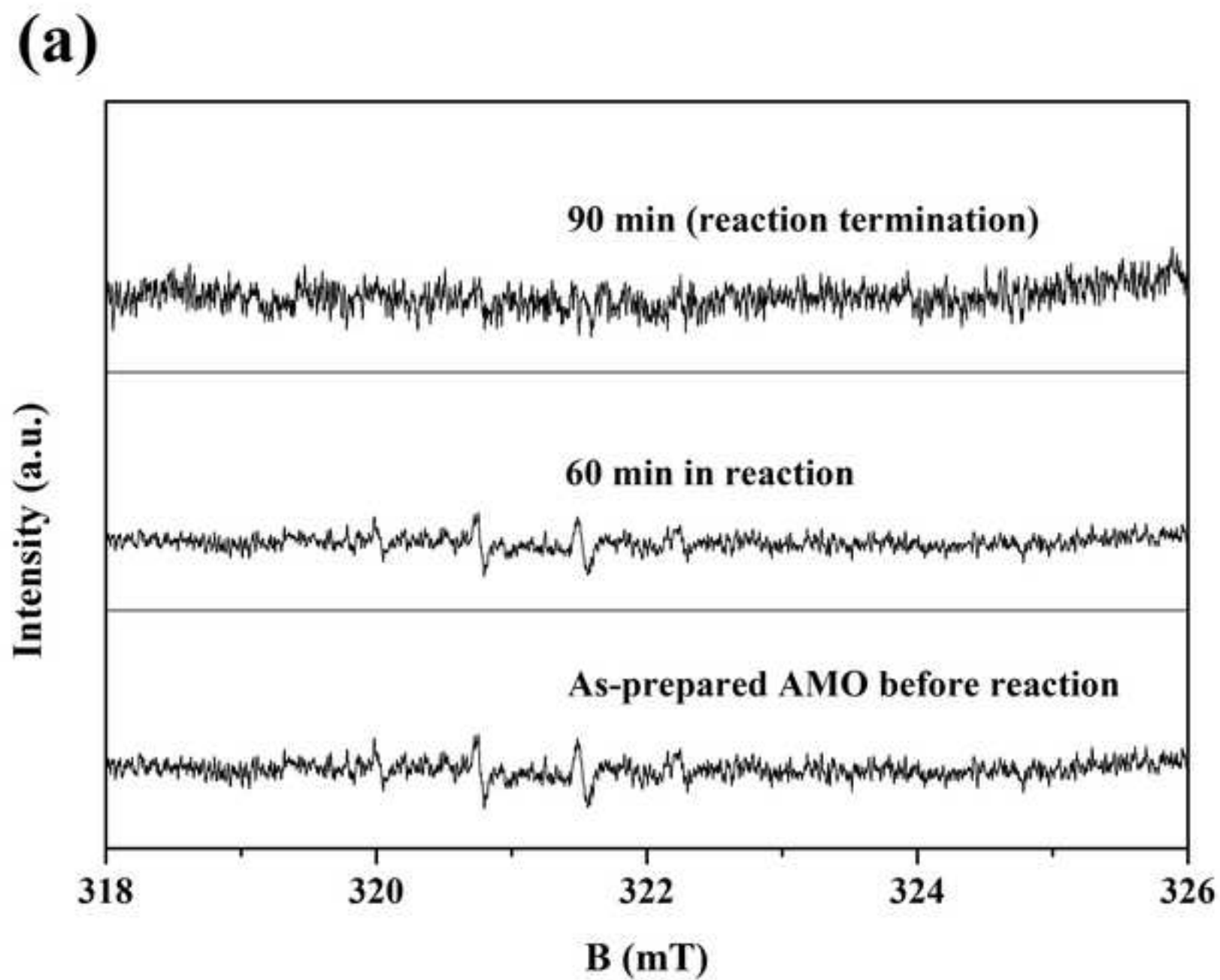


Fig. S5.b
[Click here to download high resolution image](#)

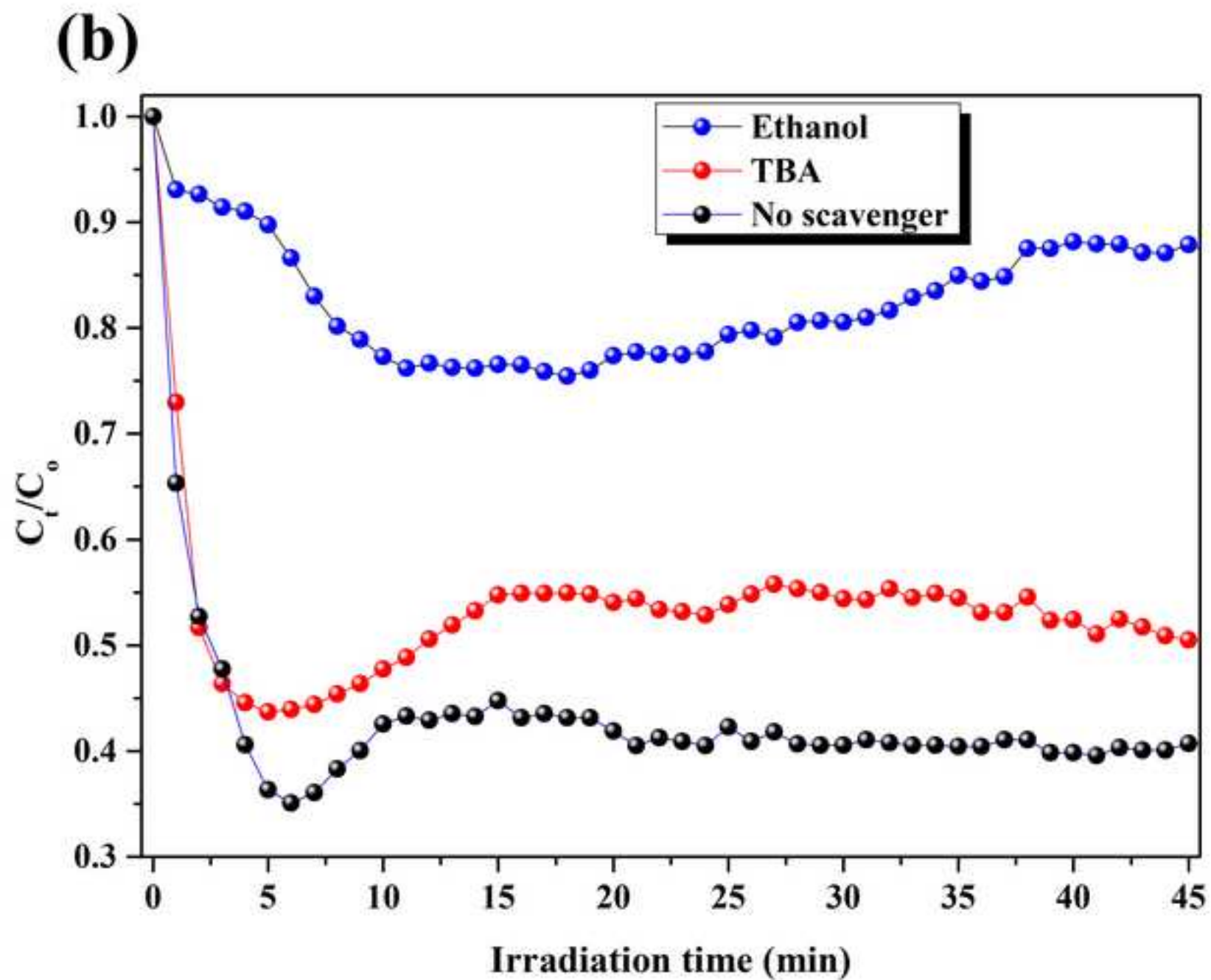


Fig. S6

[Click here to download high resolution image](#)

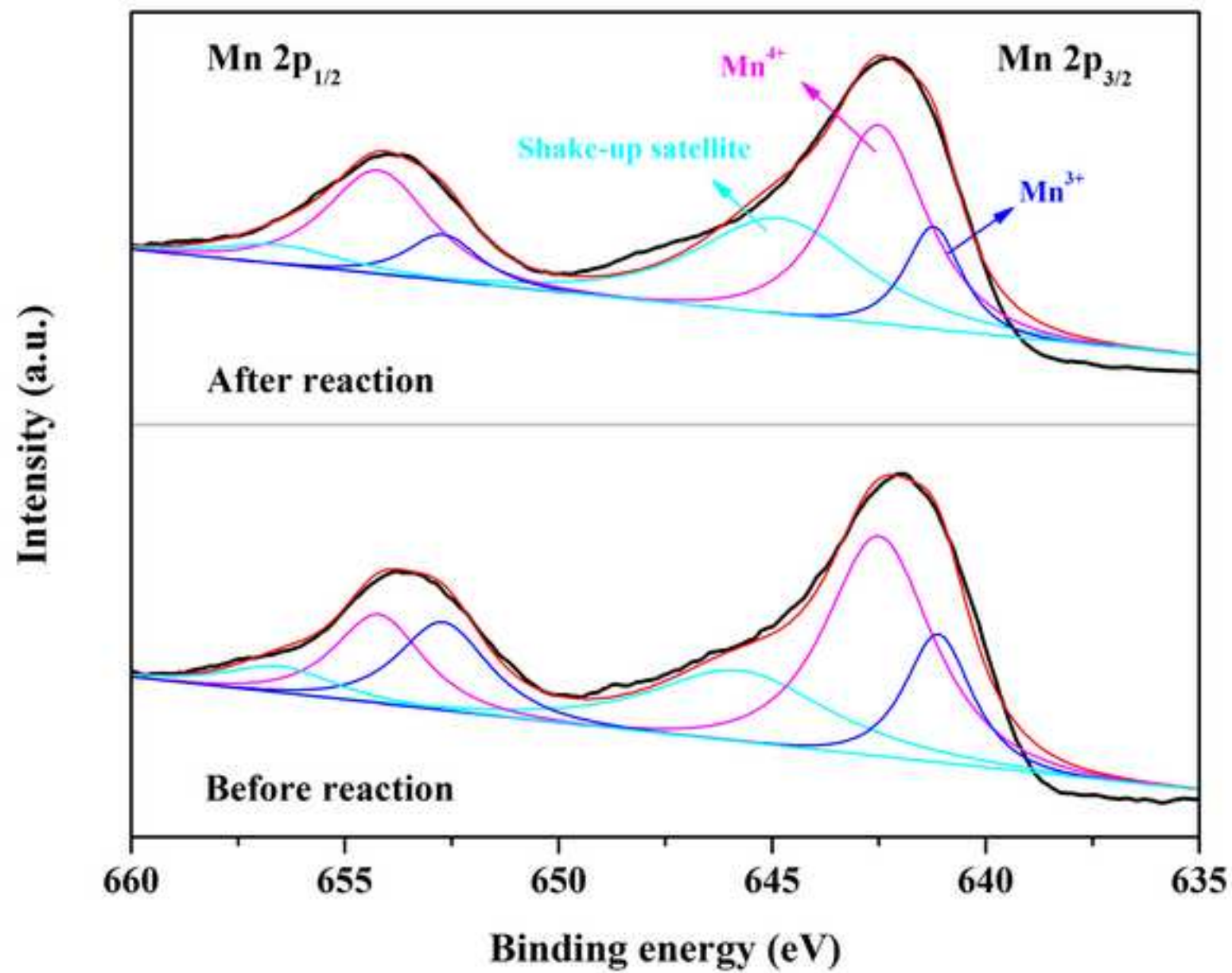
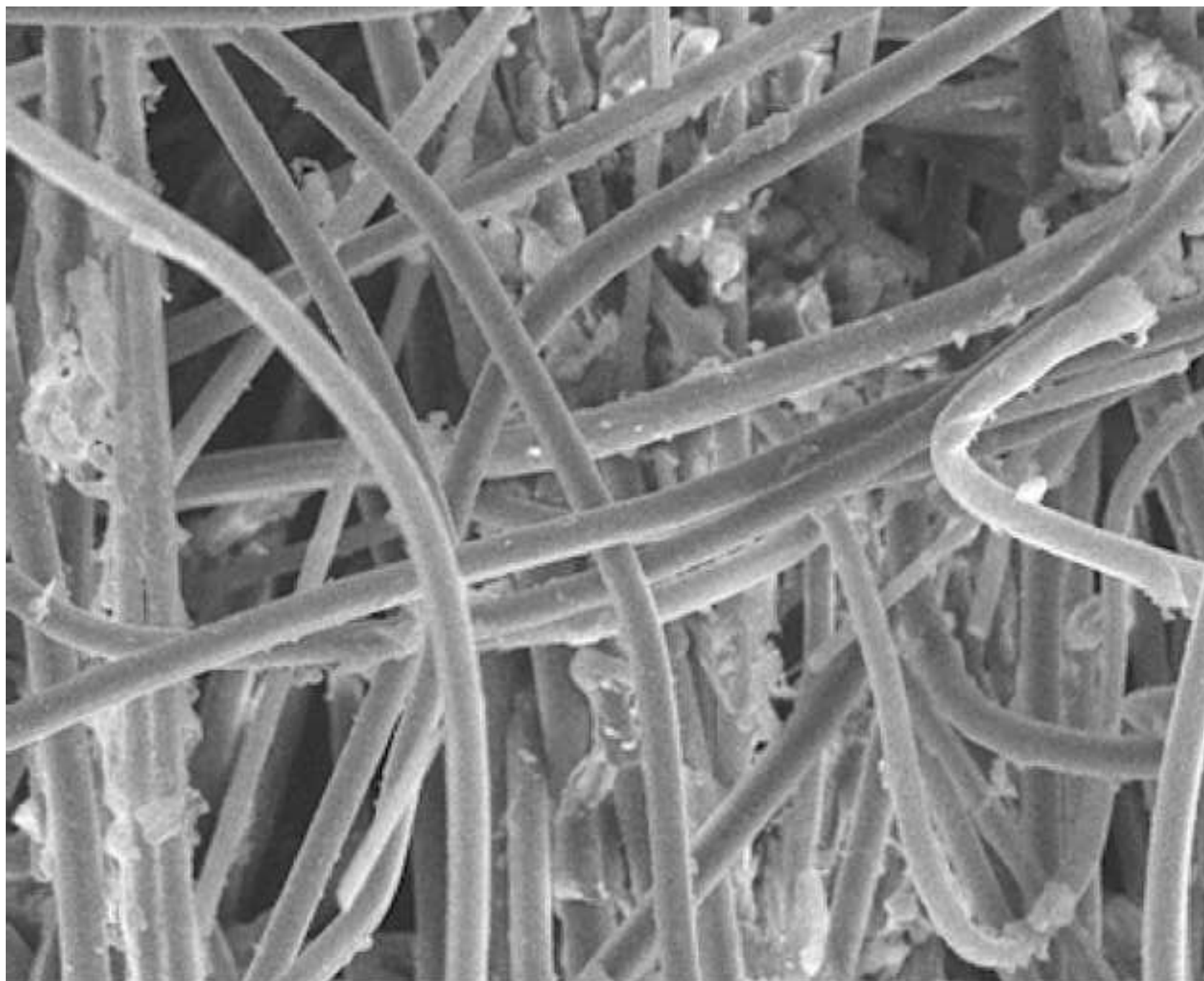


Fig. S7.a

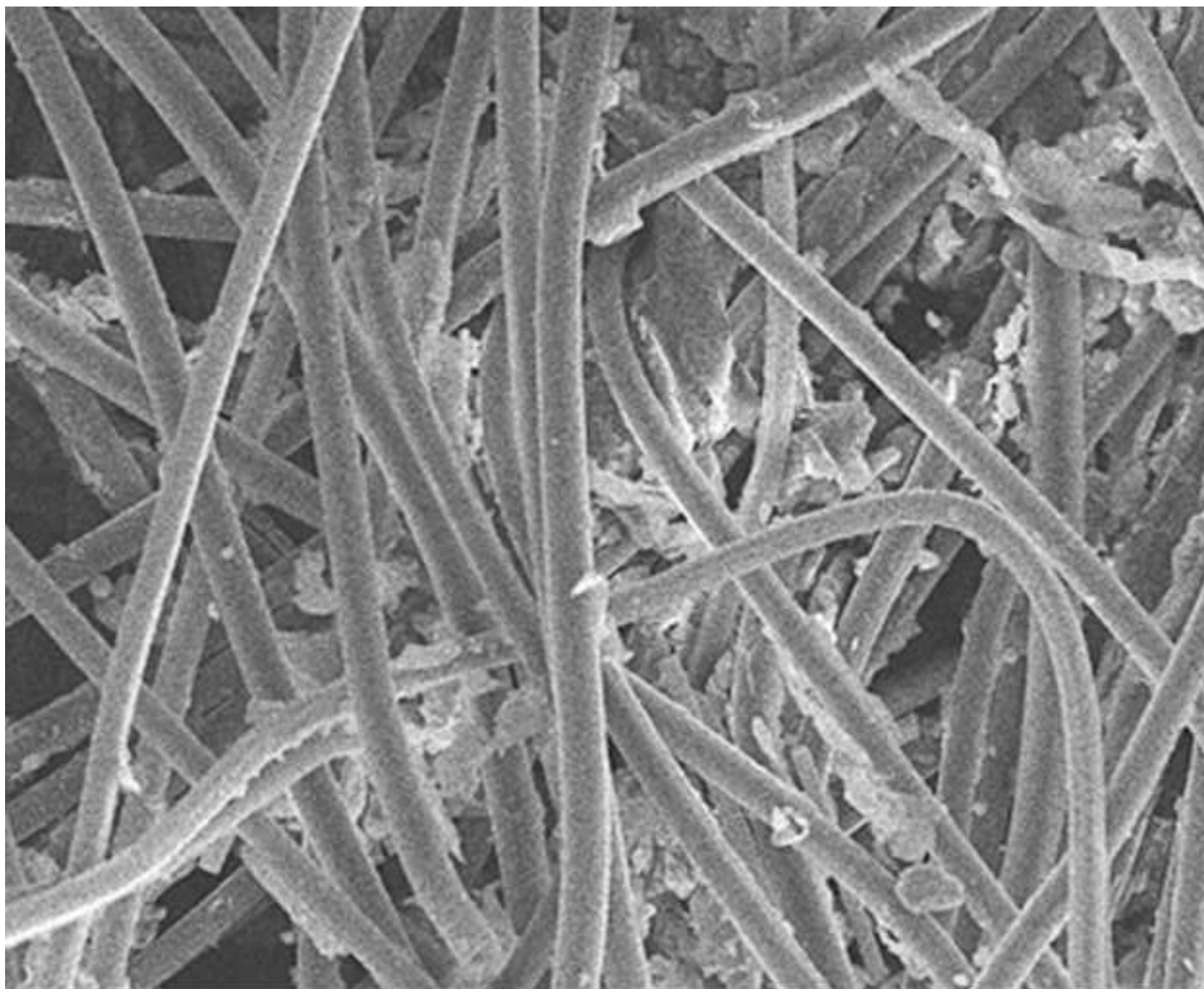
[Click here to download high resolution image](#)



(a) $k_2 = 0.24 \text{ Pa} \cdot \text{min} \cdot \text{m}/\text{mg}$

Fig. S7.b

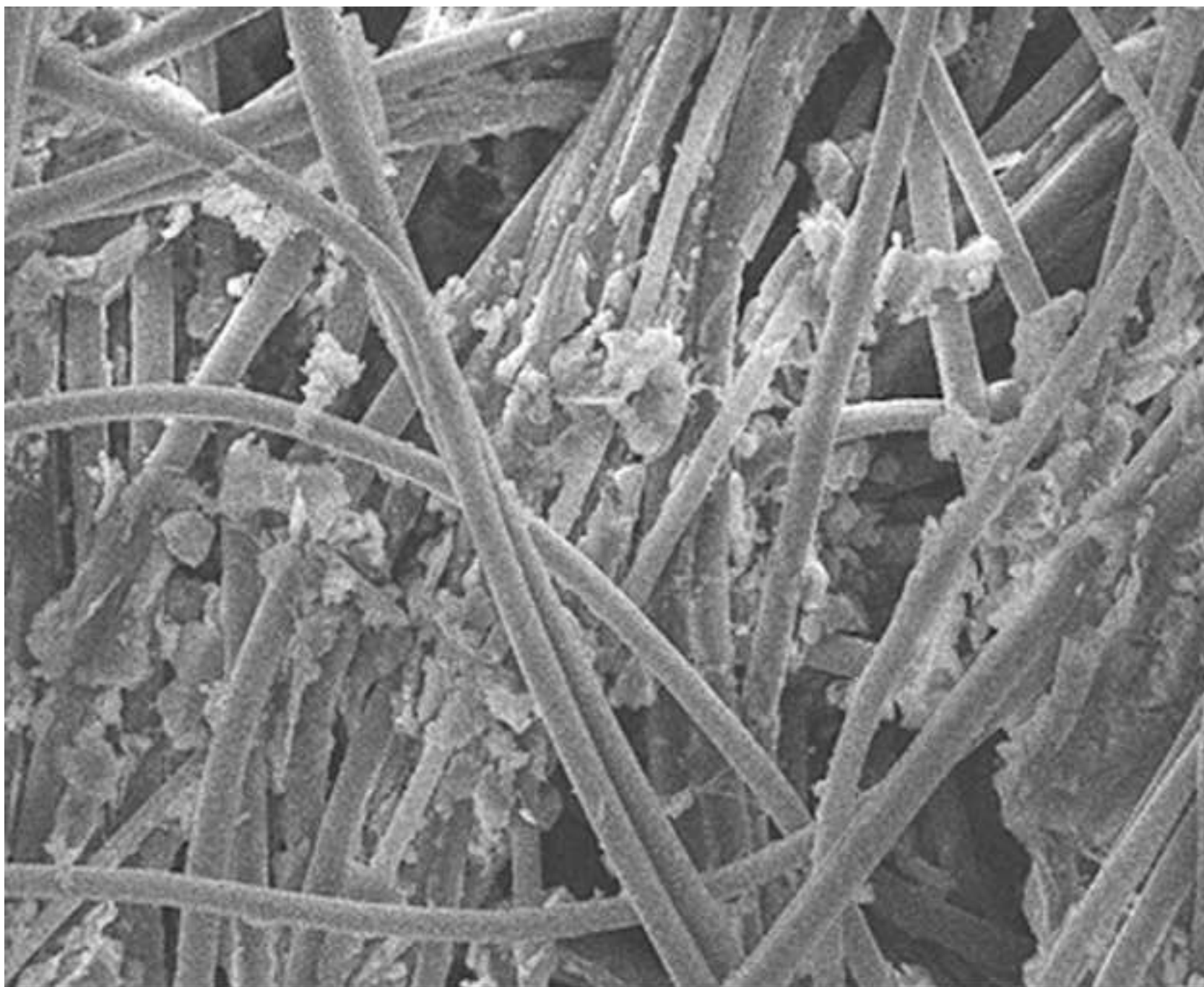
[Click here to download high resolution image](#)



(b) $k_2 = 1.49 \text{ Pa} \cdot \text{min} \cdot \text{m}/\text{mg}$

Fig. S7.c

[Click here to download high resolution image](#)



(c) $k_2 = 5.59 \text{ Pa} \cdot \text{min} \cdot \text{m}/\text{mg}$

Supplementary Material

[Click here to download Supplementary Material: Support Text_CEJ-D-16-07420R1.docx](#)